PAPER • OPEN ACCESS

Controlling quantum effects in enhanced strong-field ionisation with machine-learning techniques

To cite this article: H Chomet *et al* 2022 *J. Phys. B: At. Mol. Opt. Phys.* **55** 245501

View the article online for updates and enhancements.

IOP Publishing

Controlling quantum effects in enhanced strong-field ionisation with machine-learning techniques

H Chomet, S Plesnik, D C Nicolae, J Dunham[ID], L Gover[ID], T Weaving and C Figueira de Morisson Faria*[ID]

Department of Physics and Astronomy, University College London, Gower Street, London WC1E 6BT, United Kingdom

E-mail: c.faria@ucl.ac.uk

CrossMark

Abstract

We study non-classical pathways and quantum interference in enhanced ionisation of diatomic molecules in strong laser fields using machine learning techniques. Quantum interference provides a 'bridge', which facilitates intramolecular population transfer. Its frequency is higher than that of the field, intrinsic to the system and depends on several factors, for instance the state of the initial wavepacket or the internuclear separation. Using dimensionality reduction techniques, namely t-distributed stochastic neighbour embedding and principal component analysis, we investigate the effect of multiple parameters at once and find optimal conditions for enhanced ionisation in static fields, and controlled ionisation release for two-colour driving fields. This controlled ionisation manifests itself as a step-like behaviour in the time-dependent autocorrelation function. We explain the features encountered with phase-space arguments, and also establish a hierarchy of parameters for controlling ionisation via phase-space Wigner quasiprobability flows, such as specific coherent superpositions of states, electron localisation and internuclear-distance ranges.

(Some figures may appear in colour only in the online journal)

1. Introduction

Manipulating coherent superpositions of quantum states and nonclassical pathways has been a central question to many areas of science, such as coherent control [1–3] and quantum information [4]. Important applications include controlling chemical reactions [5] or electron dynamics in ultrafast

molecular dissociation [6–9], creating quantum switches [4, 10, 11] and enhancing nonclassicality in extended systems such as light-harvesting compounds [12, 13]. In this wide range of scenarios, decoherence must be kept at bay, so that the timescales of interest are much shorter than the decoherence times. This brings one's attention to how coherent superpositions of quantum states and nonclassical pathways may be controlled in attoscience.

Attoscience has emerged from the interaction of matter with very intense laser fields, typically of the order of 10^{13} W cm^{-2} and deals with some of the shortest time scales in nature, of the order of 10^{-18} s. These extremely short timescales bring about the possibility of controlling real-time electron dynamics [14, 15], and have triggered many applications.

---

* Author to whom any correspondence should be addressed.

Examples are subfemtosecond imaging of matter (for reviews see, e.g. [16, 17]), high-harmonic spectroscopy [18], ultrafast photoelectron holography [19, 20], attosecond electron or hole migration [21–25], and, more recently, strong-field phenomena in solids [26–29] and nanostructures [30, 31]. It has even been speculated that, in the future, laser-induced electron dynamics may lead to optoelectronic computers with switching rates 100 000 times higher than existing digital electronic systems [32–34].

Recently, it has been shown that quantum interference and nonclassical pathways play a vital role in strong-field enhanced ionisation of diatomic molecules [35]. Enhanced ionisation is known for over three decades [36, 37], and consists in an increase of at least one order of magnitude in the ionisation rate of a stretched molecule, in comparison with that of an atom with a similar ionisation potential. It has been attributed to the narrowing of the upfield potential barrier due to the presence of an adjacent, downfield potential well, and to coupled charge-enhanced resonant states. Although the phenomenon is widely known, phase-space tools, such as the Wigner quasi-probability distributions [38] have shed new light on its behaviour [35, 39, 40]. Phase-space quasi-probability distributions have found enormous success in many research areas such as quantum optics [41–43], quantum information [44, 45], chemical physics [46, 47] and cold gases [48], but are hitherto underused in attoscience (for a recent review on the overall landscape within this research field see our article [49]). Nevertheless, they provide valuable insight into the dynamics of these systems of interest and have been used to study phenomena such as strong-field ionisation [39, 40, 50, 51], rescattering [52, 53] and entanglement [54]. For recent work investigating different pathways in enhanced ionisation see [55, 56].

In 2008, *momentum gates* occurring in phase space under strong oscillating laser fields were identified [39]. These gates facilitate the flow of quasi-probability from one molecular centre to the other causing many ionisation bursts within a field cycle. These bursts were later attributed to a non-adiabatic response to the time-dependent field gradients [40, 57]. However, our previous publication [35] dispelled this notion, by showing that these momentum gates are present when there is no time dependence on the field [35], or even no field at all [58], and are primarily caused by quantum interference. The term *quantum bridge* was coined to describe this mechanism.

In the present article, we aim at controlling the pathways behind enhanced ionisation, which have been identified in [35] in a systematic way, and at interpreting our findings with phase-space arguments. Some pathways may be understood within a quasi-static, semiclassical picture, whereby the quasiprobability flows along the field gradient, with tails following equienergy curves [50, 51, 59]. Other pathways are enabled by quantum interference, which creates a bridge and provides a passage for direct intra-molecular quasi-probability flow. For a time-dependent field, one must bear in mind that the phase-space configuration also changes as time progresses. Therefore, the field can act both in favour of the cyclic

motion of the quantum bridges (and the enhanced ionisation) or against it. These different temporal behaviours depend on a wealth of parameters and may be explored in order to control strong-field ionisation. Recently, it has been shown that quantum interference plays an important role even in the semiclassical ionisation pathway [60].

Previous analyses focused on understanding the physical mechanisms behind the quantum bridges, and were restricted to a homonuclear molecular potential in the field-free setting, or under a strong static or monochromatic laser field. The initial wavepacket was taken to be an upfield or downfield localised Gaussian, or a symmetric coherent superposition thereof known as a cat state [41]. Here, we focus on how the quantum bridges can be manipulated by using different relative phases and wavepacket localisations in the initial superposition state, molecular potentials of heteronuclear type, where each well is weighted asymmetrically, and electric field configurations. This is a complex task: With a wealth of tunable parameters, such as internuclear separation, relative phase and wavepacket localisation in the initial wave packet, differing nuclear charges, laser intensity and frequency as well as the pulse shape, it necessitates optimisation techniques. Machine learning methods have been explored in a wide range of scenarios in quantum physics (see the reviews [61–63] and the recent tutorial [64]) and ultrafast photonics [65]. Recently, they have been employed in the attosecond science context to control attosecond pulses [66], retrieve the structure of a large molecule from laser-induced electron diffraction patterns [67] and to track quantum pathways within a spatio-temporal Feynman path integral framework [68].

In this work, we employ machine-learning techniques for dimensionality reduction, such as the t-distributed stochastic neighbour embedding (t-SNE) [69] and principal-component analysis (PCA) [70] to find overall trends and patterns that allow us to establish a hierarchy of parameters and classify different regimes for strong-field ionisation. Throughout, we are aided by a qualitative phase-space analysis, which allows us to understand the physics behind the patterns encountered. We first employ a model molecule in a static field as a proof of concept, and, subsequently, use time-dependent two-colour driving fields. The autocorrelation function exhibit several distinct behaviours in time, including a stepwise profile in which ionisation is switched on or off. We also provide a physical interpretation for these features.

This article is organised as follows. In section 2 we discuss our model, including its general features (section 2.1) and the physical quantities of interest (section 2.2). Section 3 is devoted to the dimensionality reduction methods and their implementation. Subsequently, in section 4 we provide a qualitative analysis (4.1) and a proof of concept (4.2) for static fields, and in section 5 we show how strong-field ionisation in two-colour fields can be optimised to produce a stepwise temporal behaviour. We commence by examining the different clusters that result from the t-SNE (section 5.1) and analyse them using physical arguments (section 5.2). Finally, in section 6 we summarize our results and provide possible outlooks for the present studies.
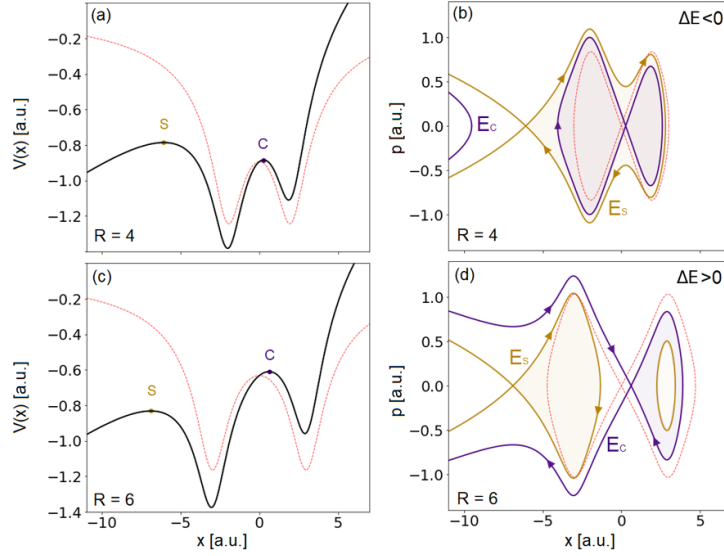
Figure 1. Effective potentials for the one-dimensional homonuclear molecular models described by the binding potentials (2), using internuclear separations of $R = 4$ and $R = 6$ and a static field $E = 0.07$. a.u. (left panels), together with the corresponding phase portraits (right panels). The Stark and the central saddles are indicated by the labels S and C in the figure, and their energy by the labels E_S and E_C. The field-free separatrices and potentials are given by the dashed red lines.

2. Model

2.1. General features

Our system is a one-dimensional single-electron molecule whose wave function dynamics $\Psi(x,t)$ are obtained by solving the time-dependent Schrödinger equation (TDSE) in atomic units using the split operator method [71]

$$i\frac{\partial}{\partial t}\Psi(x,t) = \left(-\frac{1}{2}\frac{\partial^2}{\partial x^2} + V(x) + xE(t)\right)\Psi(x,t). \quad (1)$$

The quantity $E(t)$ is the external laser field and $V(x)$ is the molecular binding potential given by

$$V(x) = Z_r V_0(x - R/2) + Z_l V_0(x + R/2), \quad (2)$$

where R is the internuclear distance. The first and second term appearing on the right-hand side of equation (2) shall be called the right and left potential wells, respectively. Each potential well $V_0(x)$ is chosen to have soft-core form

$$V_0(x) = -\frac{1}{\sqrt{x^2 + a}}, \quad (3)$$

where a is known as the softening parameter. This removes the singularity at $x = 0$ of the true Coulomb potential, yet remains long-range [72–74]. This parameter is typically chosen such that the ionisation energy coincides with the ground state of the potential [75]; throughout the following analysis $a = 1$ is chosen. Using a Gaussian wavepacket (equation (6)) with $p_0 = q_0 = 0.0$ and $\gamma = 0.5$, this softening gives the ground state energy $E_{sc} = -0.67$ a.u. for a single-centre potential [51]. For detailed discussions of quantum bridges in connection with eigenstates of the field-free Hamiltonian (and coherent superpositions thereof) see our previous work [58].

The homonuclear case is recovered by setting $Z_l = Z_r = 1$. The symbol Z is chosen in reference to nuclear charge; however, in this toy model, Z_i is allowed to be a continuous variable. Equation (3) provides qualitative insight into the behaviour of Coulomb potentials, which suffices for the objectives of the present work. Recently, however, the soft-core potential has been modified to exhibit quantitative agreement with realistic three dimensional models [76, 77].

The external laser field is either taken to be static, that is $E(t) = E_0$, or a time-dependent linearly polarised polychromatic field such that

$$E(t) = E_0\left[\cos(\omega t) + r_t \cos(b\omega t + \phi)\right], \quad (4)$$

where b is the frequency ratio between the first and the second driving wave, r_t is the field-strength ratio, ϕ is the relative phase between the two driving waves, and ω is the frequency of the fundamental.

This molecular model is analysed in phase space. There, the bound and continuum regions may be identified, and an example is shown in figure 1. Fixed points (points that satisfy $\dot{x} = \dot{p} = 0$) here are either centres or saddles [78]. Centres correspond to minima of the effective potential, and are surrounded by closed orbits. Saddles correspond to maxima of the effective potential, and delimit different dynamical regions of phase space. For instance, the central saddle separates the two molecular wells with energy E_C, and the Stark saddle is located between the downfield well and the continuum with energy E_S. The energy curves of those saddles in phase-space are called separatrices. We define the energy difference between these two saddles as

$$\Delta E = E_C - E_S. \quad (5)$$

ΔE is either negative (figure 1(a)) or positive (figure 1(c)) and characterises two different phase space configurations: closed (figure 1(b)) and open (figure 1(d)) separatrices.

The initial state of the electron $\Psi(x, 0)$ is approximated as a Gaussian wavepacket,

$$
\begin{aligned}
\Psi(x,0) &= \langle x \mid \Psi(0) \rangle \\
&= \left(\frac{\gamma}{\pi}\right)^{\frac{1}{4}} \exp\left\{-\frac{\gamma}{2}(x-q_0)^2 + \mathrm{i}p_0(x-q_0)\right\}, \quad (6)
\end{aligned}
$$

of width γ and initial momentum $p_0 = 0$. The state shall be called localised in the left well when $q_0 = -R/2$, denoted $\Psi_{\mathrm{l}}(x, 0)$, or in the right well when $q_0 = R/2$, denoted $\Psi_{\mathrm{r}}(x, 0)$, and the width γ is considered as a varying parameter in the techniques that follow. Alternatively, we may form delocalised coherent superpositions. We introduce some asymmetry between the initial left and right wavepackets in a delocalised setting. As such, the initial state in [35] is generalised by including a relative phase $\theta \in [-\pi, \pi]$ and a localisation parameter $\alpha \in [0, 1]$, giving

$$
\Psi_{\alpha,\theta}(x,0) := \frac{\sqrt{\alpha}\Psi_{\mathrm{l}}(x,0) + \sqrt{1-\alpha}e^{i\theta}\Psi_{\mathrm{r}}(x,0)}{\sqrt{1 + 2\sqrt{\alpha(1-\alpha)}\cos(\theta)\mathcal{I}_o}}. \quad (7)
$$

Under some circumstances, we also consider different widths γ_{l} and γ_{r} for the wavefunctions Ψ_{l} and Ψ_{r}, respectively. The constant of normalisation in the denominator depends on the initial state overlap $\mathcal{I}_0$:

$$
\mathcal{I}_0 = \int \Psi_{\mathrm{l}}^*(x,0)\Psi_{\mathrm{r}}(x,0)\mathrm{d}x. \quad (8)
$$

Note that $\Psi_{1,\theta}(x,0) = \Psi_{\mathrm{l}}(x,0)$ and $\Psi_{0,\theta}(x,0) = \Psi_{\mathrm{r}}(x,0)$ (up to a global phase), whilst intermediate values of α produce coherent superpositions of varying weight. If one considers $\Psi_{\frac{1}{2},0}(x,0)$ and $\Psi_{\frac{1}{2},\pi}(x,0)$, this will lead to even and odd cat states, for which the wavepacket localisation in each centre are equally weighted.

2.2. Relevant quantities

Of particular interest is the phenomenon of *enhanced ionisation*, characterised by anomalous peaks in the ionisation rate for relatively large internuclear separations. The effect is understood to arise from the presence of strongly coupled charge resonant states in combination with a narrowing of the effective potential for the upfield charge centre [36, 37]. The latter is a result of the neighbouring downfield centre enabling efficient population transfer from upfield to the continuum. The ionisation rate Γ from time $t = 0$ to $t = T$ is quantified using

$$
\Gamma = -\ln\left(\frac{|\mathcal{P}(T)|^2}{|\mathcal{P}(0)|^2}\right)\frac{1}{T}, \quad (9)
$$

where $\mathcal{P}(t)$ is the probability function at t, given by

$$
\mathcal{P}(t) = \int_{-\infty}^{+\infty} \Psi^*(x,t)\Psi(x,t)\mathrm{d}x. \quad (10)
$$

This definition of ionisation rate was used in the seminal paper [36] in the context of enhanced ionisation of molecules. Numerically, the integral limits of equation (10) are finite, taken throughout the box of size $x = -100$ to $x = 100$ a.u. Because of irreversible ionisation equation (10) will decrease with time and be less than unity. No absorber was used, and reflections are minimised by using a total grid size twice as large as the box size. The final time is chosen to be $T = 150$ a.u. as it has been used in previous publications [35, 49, 58]. Throughout, Γ will be written in arbitrary units.

Equation (9) will be employed throughout in order to test our optimisation methods for static fields. The static field in this work is chosen in such a way that the left well is located downfield and the right well upfield.

Another relevant quantity, which provides insight into the resulting wave function dynamics, is the autocorrelation function

$$
a(t) = \int \Psi^*(x,t)\Psi(x,0)\mathrm{d}x, \quad (11)
$$

which is given by the overlap integral between the initial and time propagated wave function. The autocorrelation function will be employed to assess the behaviour of the system in time-dependent electric fields.

The Wigner quasi-probability distribution [38] is a useful tool in the analysis of phase-space dynamics (for a review see [79]). It is defined as

$$
W(x,p,t) = \frac{1}{\pi}\int_{\infty}^{-\infty}\mathrm{d}\xi\Psi^*(x+\xi,t)\Psi(x-\xi,t)\mathrm{e}^{2ip\xi}. \quad (12)
$$

The Wigner function is real and normalised, with the property that its marginals correspond to physical probability distributions for each conjugate variable, respectively. $W(x,p,t)$ may assume negative values, and this can provide an indication of nonclassicality [80].

3. Dimensionality reduction

The present problem depends on many parameters: The initial wavepacket localisation α, its widths γ_{l} and γ_{r} and relative phase θ; molecular parameters like the weights Z_{l} and Z_{r} and the inter-nuclear distance R; and many external electric-field parameters such as ϕ, r_t, b and E_0. The main challenge to overcome when studying the effect of a large number of parameters simultaneously is how to visualise the results. Indeed, each data point will exist in a high-dimensional space (the number of dimensions equal to the number of parameter used), and ideally we would like to project our results down to a two-dimensional space.

To this end we will use t-SNE, an unsupervised dimensionality reduction technique, meaning it will find overall trends and patterns without any prior knowledge on the origin of the data. A detailed explanation of the workings of the t-SNE method can be found in [69], and its main steps are summarised here:
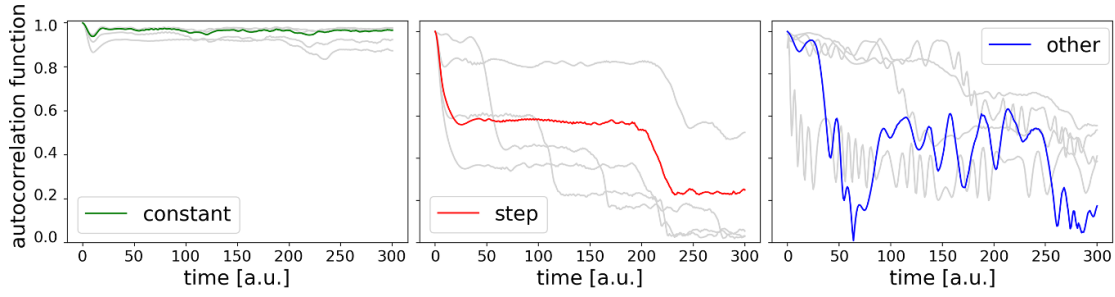
Figure 2. Examples of the three potential outputs of the autocorrelation function sorting algorithm. The parameters used vary greatly but are all within the range shown in table 1.

(a) Defining a probability distribution p_{ij} of picking a pair of points (x_i, x_j) in our original high dimensional space such that neighbouring points lead to a higher probability. This is done by defining the conditional probability $p_{i|j}$ of a point x_j being picked after choosing x_i by

$$p_{i|j} = \frac{\exp(-||x_i - x_j||^2)/2\sigma_i^2}{\sum_{k \neq i} \exp(-||x_i - x_k||^2/2\sigma_i^2)}. \quad (13)$$

The conditional probability is represented by a Gaussian distribution of the Euclidean distance between points x in high dimensional space. The Gaussian is centred at x_i, has standard deviation σ_i, and is normalised in order to handle clusters of different densities. The conditional probability $p_{i|i} = 0$. From these conditional probabilities we create the joint distribution p_{ij}

$$p_{ij} = \frac{p_{i|j} + p_{j|i}}{2n} \quad (14)$$

where n is the number of data points.

(b) Creating a random dataset of points χ in the target dimension and calculating, similarly to step 1, the joint probability distribution q_{ij} of picking a pair of points (χ_i, χ_j)

$$q_{ij} = \frac{(1 + ||\chi_i - \chi_j||^2)^{-1}}{\sum_{k \neq l}(1 + ||\chi_k - \chi_l||^2)^{-1}}. \quad (15)$$

However, instead of a Gaussian distribution, q_{ij} is represented by the Student's t-distribution with one degree of freedom (equivalent to a Cauchy distribution), which is much more heavy-tailed.

(c) Modifying the dataset χ in the target dimension such that q_{ij} is as similar as possible to p_{ij}. This is done by defining a cost function C

$$C = \mathrm{KL}(P||Q) = \sum_i \sum_j p_{ij} \log \frac{p_{ij}}{q_{ij}} \quad (16)$$

chosen to be the Kullback–Leibler divergence (KL divergence) [81] between the two distributions. The KL divergence is a measure of how different two distributions are to one another. We then minimise the cost function C using the gradient descent method. This involves taking

a stochastic sampling of the cost function and obtaining the gradient

$$\frac{\delta C}{\delta \chi_i} = 4 \sum_j (p_{ij} - q_{ij})(\chi_i - \chi_j)(1 + ||\chi_i - \chi_j||^2)^{-1} \quad (17)$$

for a small batch of samples. The gradient is then scaled by the learning rate (often referred to as step size) and used to modify the target dataset χ. This procedure is then repeated over many steps, which approximates the true gradient and successfully minimises the cost function. For a more detailed explanation of the stochastic gradient descent method see [82].

As a reality check, we will compare all t-SNE projections to PCA [70] dimensional reduction. Indeed, t-SNE is stochastic, so each run can yield different results. It focuses on preserving the local structure of the data and is a non-linear technique. On the other hand, PCA is linear, deterministic, and preserves global properties while potentially losing low-variance deviations between neighbours. Therefore by comparing both projections we can guarantee the accuracy of the t-SNE results. For clarity, some key results obtained with the PCA are given in the appendix. To make use of the t-SNE capabilities we need to include information about the wavefunction in the static field case or its evolution in the time-dependent case.

3.1. Time evolution characterisation

In order to understand the system dynamics through the use the dimensionality reduction methods, we wish to characterise the electronic dynamics by a single value. In the static-field case we will employ the ionisation rate Γ (9). For the time-dependent case we choose to quantify the shape of the autocorrelation function (11), as it carries more temporal information. A preliminary investigation showed that the autocorrelation function can take three distinct shapes (figure 2): 'steps', 'constant', and 'other', which represent different behaviours.

The classification of autocorrelation functions into the defined categories is performed by a simple deterministic decision tree algorithm. First, we check whether a function is 'constant', that is, if it does not fall below a given threshold value. Next, we look for the steps. Steps are characterised by

Table 1. Table of all parameters used throughout this paper with the minimum and maximum value of the range they are randomly chosen from.

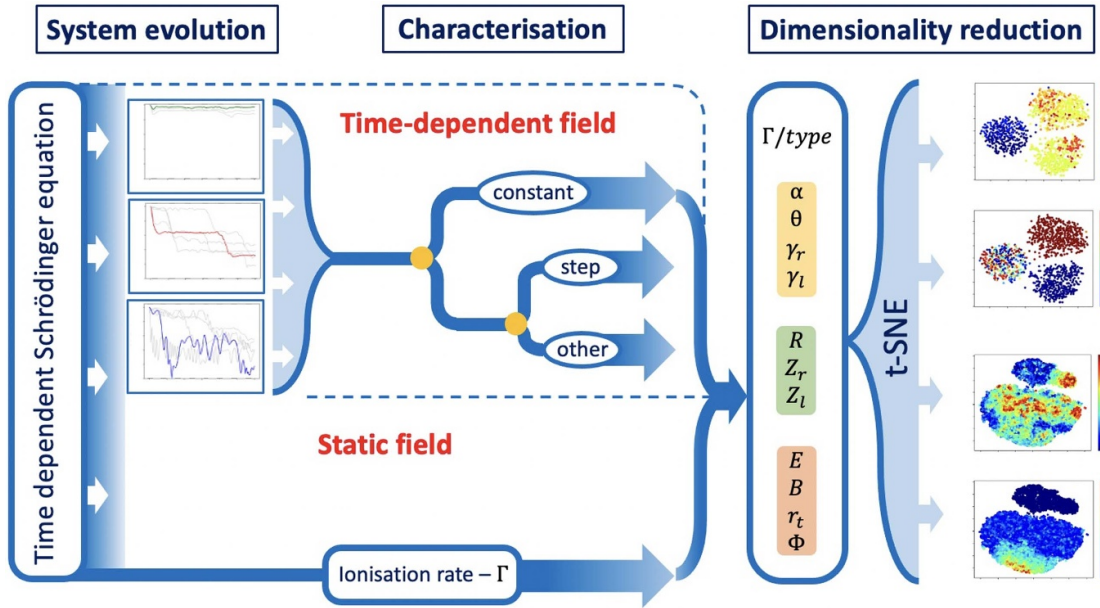| Static Field	α	θ	γ_r	γ_l	R	Z_r	Z_l	E_0			
Min	0.0	0.0	0.2	0.2	3.0	1.0	1.0	0.04			
Max	1.0	π	1.0	1.0	12.0	2.0	2.0	0.08			
Time-dependent Field	α	θ	γ_r	γ_l	R	Z_r	Z_l	E_0	b	r_t	ϕ
Min	0.0	0.0	0.2	0.2	4.0	1.0	1.0	0.04	0.5	0.0	$-\pi$
Max	1.0	π	1.0	1.0	10.0	1.5	1.5	0.08	2.0	1.0	π

Figure 3. Schematic outline of the methodology used throughout the paper.

the intervals where the autocorrelation function stays approximately constant, followed by a steep decline. Hence, if we find a constant interval longer than some 'critical length', we categorise it as a 'step'. We define a constant interval as an interval where the difference of any two values is smaller than a critical threshold, 'ε'. If the function is not caught by these checks, it is classified as 'other'. In the results presented in section 5 the threshold value is set to 0.8, the critical length is set to 100, while the critical ε is 0.03. All of the autocorrelation function arrays used have 3000 elements.

3.2. Method

To obtain a data point, $N-1$ parameters are randomly uniformly distributed within the range shown in table 1. The electronic wavefunction is then evolved using the TDSE and we characterise the time evolution information by a single value as described in the above section. In case of a static external field studied in section 4 this is done by computing the ionisation rate Γ (equation (9)). For the time-dependent field in section 5 we quantify the shape of the electron autocorrelation function (see section 3.1). The $N-1$ parameters chosen randomly as well as the single value characterising the time evolution form a data point of size N.

In certain situations specific data points are removed from the final data set in order to focus the visualisation on the matter at hand. For example in section 5.1, only 1332 data points are used from the 1 million originally computed using random parameters. Indeed, in order to focus on the 'step' output of the autocorrelation function, approximately 99.9% of data points with outputs 'constant' and 99.97% of data points with output 'other' are removed.

We then use the t-SNE to reduce our N-dimensional data points to 2 dimensions, projecting the data set onto the two axis y_1 and y_2. Because the t-SNE is inherently nonlinear, it is not possible to reverse-transform its output to the original dataset. Therefore, these axes have no clear meaning with relation to the original dataset and they act solely as two dimensions in which the results are visualized. The implementation of the t-SNE algorithm is scikit-learn, and has time complexity of $O(n^2)$ where n is the number of samples. The data points will have clustered into different groups, the nature of which will be understood by plotting the projection as a function of one of the input parameters. This will allow us to determine which parameter or which combination of parameters influence the ionisation rate or the autocorrelation function step, and to what degree. The overall method described here and used throughout this paper is summarised schematically in figure 3. Finally,

J. Phys. B: At. Mol. Opt. Phys. **55** (2022) 245501

H Chomet *et al*

the PCA method is used to ensure that the observed behaviour is neither a remnant of the stochastic nature of the algorithm, nor due to the removing of data points from the data set. Examples of PCA results are shown in the appendix.

4. Static fields

We will start our study with an analysis of enhanced ionisation in static fields. While the ultimate goal is to understand and control enhanced ionisation in time-dependent fields, the purpose of this static field section is two-fold:

- Obtain an in depth understanding of how certain parameters influence the system, and expand on the conclusions drawn in [35, 49].
- Establish the effectiveness of the t-SNE dimensionality reduction technique as a method of simultaneous multi-parameter analysis. This will allow us to use it as a primary tool in section 5.

4.1. Qualitative analysis

As a starting point, we will perform a qualitative investigation of how specific parameters influence the quantum bridges and the ionisation rate in a static field using the generalised initial wavepacket given by equation (6). We employ phase-space arguments and Wigner functions to facilitate the interpretation.

4.1.1. Initial electron wavepacket. Our earlier work on the subject [35] led to the conclusion that a major predictor of enhanced ionisation was the localisation of the initial electron wavepacket. However, only three configurations were studied: localised around the right well, localised around the left well, and delocalised equally around both centres. Here we start with a more thorough analysis of this parameter by considering it a continuous variable, α, see equation (7). As shown in figure 4, the ionisation rate is linearly proportional to the electron localisation, with $\alpha = 0.0$ (initially localised upfield) leading to the highest ionisation rate. This can be understood as the downfield centre narrowing the effective-potential barrier for the upfield centre, hence enhancing upfield ionisation.

In addition to a continuous localisation parameter, the state of the initial electron wavepacket is varied by a relative phase factor θ, see equation (7), between the superposition of Ψ_r and Ψ_l. When using an equally delocalised wavepacket, $\alpha = 0.5$, the ionisation rate as a function of θ (in rad) peaks around $\theta = 2.4$ and is minimal for $\theta = -0.8$. This has little overall influence on the ionisation rate as seen in figure 4. Finally, the initial wavepacket widths γ_r and γ_l, see equation (6), are set to differ from $\gamma = 0.5$, which gives the minimal ground-state energy of a field free single-centre soft-core potential with softening parameter $a = 1.0$. This has no major influence on the ionisation rate and is not shown here.
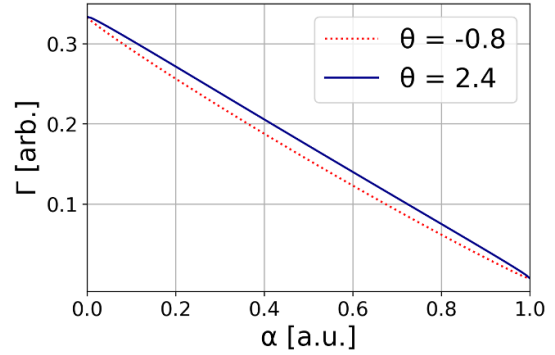

Figure 4. Ionisation rate Γ for an initial wave packet $\Psi_{\alpha,\theta}(x,0)$ with respect to the localisation parameter α, comparing maximum $\theta = 2.4$ and minimum $\theta = -0.8$. The external static field has strength $E_0 = 0.06 a.u.$, and the molecular parameters used are internuclear distance $R = 7$ a.u., $Z_r = 1.0$ and $Z_l = 1.0$
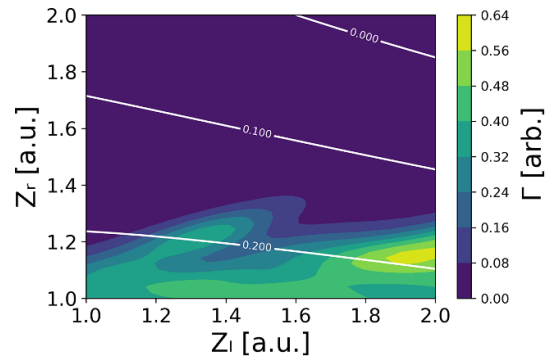

Figure 5. Contour plot of the ionisation rate Γ as a function of Z_l and Z_r using an external static field $E_0 = 0.06 a.u.$ with internuclear distance $R = 7$ a.u. The white lines indicate the separatrix energy difference ΔE, with the 0.0 line indicating the transition from open separatrices ($\Delta E > 0$) to closed separatrices ($\Delta E < 0$).

4.1.2. Heteronuclear molecule $Z_{l,r}$. Finally, we expand our study to include heteronuclear molecules. We analyse the ionisation rate while varying the value of molecular weights Z_r and Z_l, of equation (2). The study of heteronuclear molecules is motivated by enabling a change in the critical internuclear distance where the phase-space separatrices change configuration and in the dynamics of the quantum bridges. From figure 5 studying the ionisation rate as a function of both charges Z_r and Z_l simultaneously shows a large region of suppressed ionisation as $Z_r > 1.3$. The effect of Z_l is a lot less pronounced, leading to high ionisation rates even at $Z_l = 2.0$. While open separatrices do not guarantee a high ionisation rate, closed separatrices always suppress ionisation. To have a better understanding of the sharp decrease in ionisation rate with respect to Z_r, we look at the Wigner quasi-probability distribution in figure 6. Comparing the bound region around the right molecular centre in (a) and (b), as Z_r increases, the right molecular well deepens greatly. This leads the upfield population to stay trapped and greatly suppresses ionisation. On the other hand, the increase of the left bound region in (c) due to an increase in
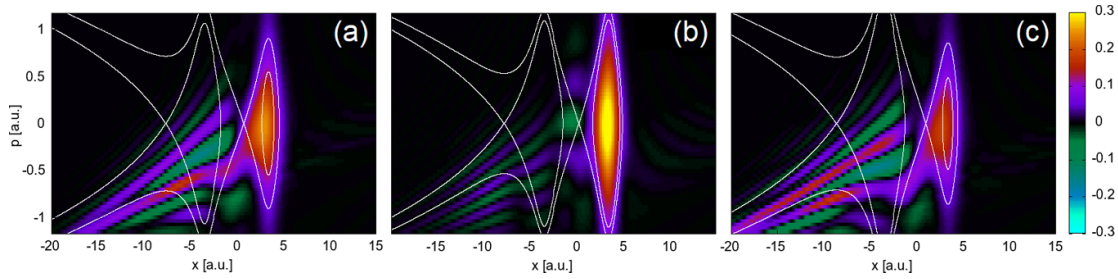
J. Phys. B: At. Mol. Opt. Phys. **55** (2022) 245501

H Chomet *et al*

Figure 6. Wigner quasi-probability distribution of the ionisation from a static field $E_0 = 0.06\,a.u.$ with internuclear distance $R = 7$ for (a) $Z_r = 1.0$ and $Z_l = 1.0$, (b) $Z_r = 1.5$ and $Z_l = 1.0$ and (c) $Z_r = 1.0$ and $Z_l = 1.5$ a.u.. The snapshots are taken at $t = 25$ a.u..
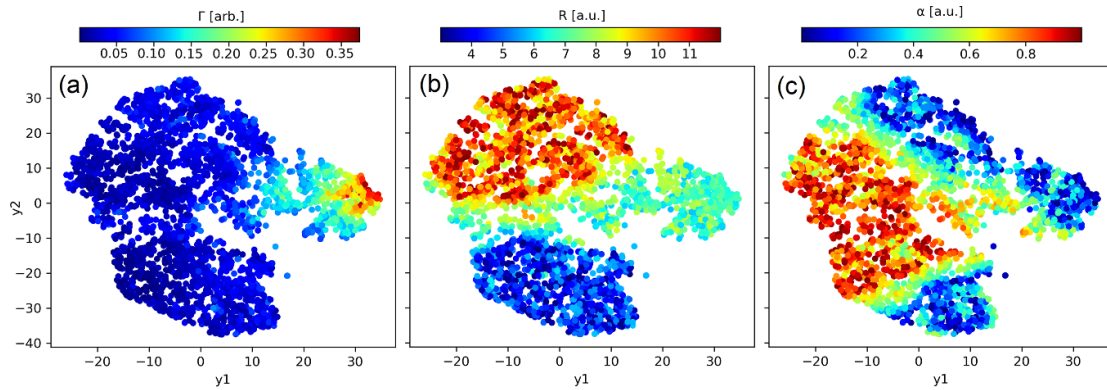

Figure 7. Plot of the 3000 6-dimensional data points that have been projected onto two axis y_1 and y_2 using the t-SNE dimensional reduction technique described in section 2.2. Each subplot has the projected data plotted as a function an initial input parameter. The initial input parameters include (a) the ionisation rate Γ (given in arbitrary units), (b) the internuclear distance R, (c) the electron localisation α. Also included but not shown here are the left initial wavepacket width γ_l, the right wavepacket width γ_r and the phase difference between the left and right initial wavepackets θ. PCA distributions using the same data points have been analysed for accuracy (not shown). The external field is taken to be static with $E_0 = 0.0534$ a.u. and the molecular weights $Z_r = 1.0$ and $Z_l = 1.0$, matching the results from [35].

Z_l does not greatly influence the ionisation rate. This is because in enhanced ionisation the majority of the ionised population comes from the upfield centre, as shown in [35]. There is very little change to the upfield (right-hand-side here) centre when increasing Z_l.

Now, a more complete overview would go through the effect of Z_l and Z_r with respect to various parameters, which would be slow and exhaustive. Instead we propose in the following section to use dimensionality reduction techniques to analyse the effect of multiple parameters at once.

4.2. Proof of concept—machine learning techniques

We now aim to study the effect of multiple parameters on the ionisation rate, starting with a limited number in order to fully understand the results and to focus on the effect of the chosen parameters. Those are the internuclear distance R, the width of the initial superposed gaussian upfield and downfield wavepackets γ_l and γ_r, the phase difference θ between them, and the localisation parameter of the wavepacket α. The value of these parameters is chosen from a predetermined range described in section 3.2.

Data points comprised of these five parameters as well as the ionisation rate are projected onto two axis y_1 and y_2 using the t-SNE algorithm, shown in figure 7. As is

explained in section 3.2, the projection axes y_1 and y_2 are not straightforwardly interpretable in terms of the original dataset and are meant for visualisation only. This method is described in section 3.2.

From figure 7, we see that the projected data bring into focus the connection between the ionisation rate, the internuclear distance and the electron localisation. These match the results from [35] and section 4.1. That is, peak ionisation yield is present at and around the peak internuclear distance of $R = 6.8$ a.u., shown in figure 7(b), and when the initial wavepacket is localised upfield, shown in figure 7(c). The low ionisation rate regions, seen in figure 7(a), split into two distinct parts seen in figure 7(b) which correspond respectively to regions of too low and too high internuclear distance, studied in depth in [35]. The ionisation rate falls linearly as the electron localisation changes from localised upfield to localised downfield, as seen in figure 4. The effect of the gaussian widths γ and the phase difference θ is a lot weaker than those discussed above, and are not shown here.

We will now look at the full range of parameters. In addition to the previous six, these following results will include the effects of the nuclear weight number Z_r and Z_l, and the electric field strength E_0. Because of these additional parameters, we posit that there is no longer a clear internuclear distance peak, but instead a larger range of optimal internuclear distances,
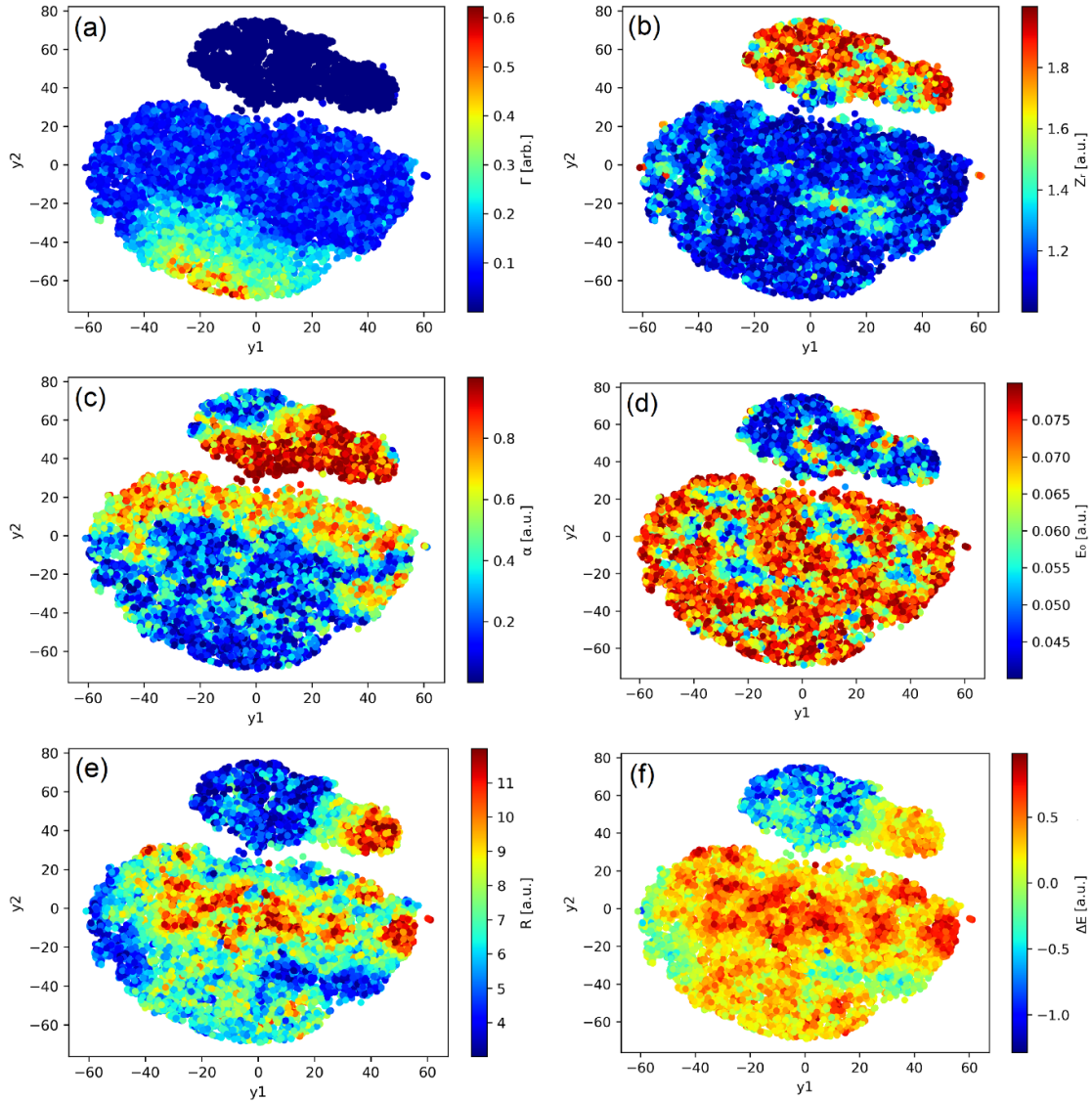
Figure 8. Plot of the 16 995 9-dimensional data points that have been projected onto two axis y_1 and y_2 using the t-SNE dimensional reduction technique described in section 2.2. Each subplot has the projected data plotted as a function an initial input parameter. The initial input parameters include (a) the ionisation rate Γ, (b) the right molecular well depth Z_r, (c) the electron localisation α, (d) the field strength E_0, (e) the internuclear distance R. Also included but not shown here are the left molecular well depth Z_l, the left initial wavepacket width γ_l, the right wavepacket width γ_r and the phase difference between the left and right initial wavepackets θ. In subplot (f) the separatrix energy difference ΔE is shown for each data point, however it is not one of the input parameters. The input data set has been reduced from 100 000 data points to only have either $\Gamma < 0.002$ or $\Gamma > 0.05$. PCA distributions using the original 100 000 data points are shown in appendix.

dependent on E_0, Z_r and Z_l. For that reason the difference in energy between the central and Stark separatrix ΔE will also be analysed, but will not be an input parameter.

As seen in figure 8(a), the algorithm successfully separates two clusters of low ($\Gamma < 0.002$) and high ($\Gamma > 0.05$) ionisation yield. Within the high ionisation cluster, the data points are further distinguished by a very high ($\Gamma > 0.3$) ionisation yield region. From the distribution of other parameters in these two clusters, we can determine which lead to a high ionisation yield.

The strongest predictor of high ionisation rate is the nuclear depth factor Z_r, (see figure 8(b)), which in this configuration is associated to the upfield molecular well. As shown in figure 5,

the ionisation rate falls of sharply as soon as $Z_r > 1.0$. While the value of Z_r is originally chosen randomly in the range [1:2], the average value of Z_r in the high ionisation yield cluster is 1.16, and 1.12 in the $\Gamma > 0.3$ region. Indeed, 90% of the $\Gamma > 0.3$ ionisation yield data points have $Z_r < 1.25$.

In figure 8(c), echoing the conclusions from figures 4 and 7, only 4% of the high ionisation yield data points have the initial wavepacket of the electron localised downfield, with $\alpha > 0.8$. Similarly, 30% of the high ionisation yield cluster data points are for an initial wavepacket localised upfield, with $\alpha < 0.2$. This proportion goes up to 72% for $\Gamma > 0.3$.

From figure 8(d), the median initial field strength E_0 of the high ionisation yield cluster is 0.07, despite the parameter

being originally randomly chosen from a [0.04:0.08] range. This means the majority of high ionisation yield data points have a high field strength. Indeed, 82% of data points have $E_0 > 0.06$ a.u. in that cluster and 88% in the $\Gamma > 0.3$ region.

As hypothesised earlier, the clear internuclear distance peak from figure 7 is now less pronounced in figure 8(e) as we are now also varying the molecular weights Z and the field amplitude E_0. Still, 72% of data points within the very high, $\Gamma > 0.3$, ionisation yield region have internuclear distances R in the range $6 < R < 9$. This is surprising as the initial range for R is randomly taken from [3:12]. Therefore, one would expect that one third of the data points would be in this range.

Finally, in figure 8(f), we can deduce the effect of the separatrices on the ionisation yield. Indeed if the separatrices are nested (see figure 1), meaning that $E_S > E_C$, or $\Delta E < 0$, then the ionisation rate is suppressed. In contrast, 99.5% data points in the high ionisation yield cluster have $\Delta E > -0.5$, and 86% of them have $\Delta E > 0$. This separation is present despite ΔE not being used as an input parameter.

In conclusion, the t-SNE enables us to visualise the effect of multiple parameters simultaneously. All the conclusions drawn in section 4.1 are visualised in figure 8. Parameters with little to no effect are swiftly identified and separated from relevant parameters. Not only that, but a hierarchy of the effect of different parameters is also established much more rapidly. For example the effect of Z_l on the ionisation rate being greater than that of α. Because of this we will be able to use the t-SNE in the following section to rapidly assert what parameters are relevant and to what degree.

5. Time dependent fields—control of enhanced ionisation—optimising autocorrelation step function

When using a polychromatic field (see equation (4)) and specific parameters, we can obtain a 'controlled' ionisation release, which translates to a step function in the autocorrelation function plot. In the following section we will be looking at what parameters lead to step functions and why specific configurations lead to a controlled ionisation release.

5.1. t-SNE application to step functions

5.1.1. The 3 clusters and electron localisation. The t-SNE algorithm separates the data into three different clusters, whose nature can be seen in the two plots of figure 9. Therein, the data points are coloured with respect to (a) their autocorrelation function type and (b) their initial electron localisation α. Indeed, one cluster groups all autocorrelation functions classified as 'constant' or 'other', while the other two contain the autocorrelation functions classified as 'steps'. Those two clusters are understood by looking at the distribution with respect to the initial electron localisation. All autocorrelation functions that are classified as 'steps' have their initial electron wavepacket localised completely at one centre. The clusters are separated between having the initial electron wavepacket localised at the left centre ($\alpha > 0.95$, or dark red) and localised

at the right centre ($\alpha < 0.05$, or dark blue). From this it is clear that the initial wavepacket must be localised either to the left or to the right for there to be steps. This is explained when looking at figure 14, in section 5.2.1.

5.1.2. Difference between the two 'step' clusters and the 'other' and 'constant' cluster. From looking at the different clusters, we can find other correlations, shown in figure 10, between certain parameters and the presence of step functions. most notably, the field ratio r_t between the two driving waves, in subplot (a). Indeed, while originally the value of r_t is chosen randomly from a range [0:1], the two step clusters have a median r_t value of 0.81 and an average of 0.75. Moreover, longer step lengths (more than 150 a.u., or orange/red) have a r_t median value of 0.85 and an average of 0.8.

Next, the overall electric field strength E_0, chosen at random from a range of [0.04:0.08], has an median and average value of $E_0 = 0.07$ a.u.. These can be understood as by seeing that both a high field ratio r_t and a high field strength E_0 lead to a higher field peak during which more of the population will escape, causing a deeper drop in the autocorrelation function.

Finally, the internuclear distance is clearly closer to the peak internuclear distance of $R = 7$ a.u., which is also confirmed by the standard deviation being only 1.05 instead of 1.3. R is also for 92.6% of all data in the step clusters above a minimum internuclear distance of $R = 6$ a.u.. The cause of this effect is more complex, and is discussed in detail in section 5.2.2.

5.1.3. Symmetry between the 'localised to the left' and 'localised to the right' step clusters. The value of α is not the only difference between the two step clusters. The next series of parameters, shown in figure 11, are connected to the symmetry between the left and right molecular wells. First, there is quite naturally the distribution of γ_l and γ_r. From their definition in equation (6), γ_l only influences the initial wavepacket localised to the left. Therefore, if the initial wavepacket was localised to the left, only the initial left wavepacket width γ_l is a relevant parameter, and vice versa. Since, as shown in figure 9, both step clusters use initially localised wavepackets exclusively, only one γ parameter influences each cluster and the θ parameter (subplot (a)) has no effect on them. As seen in figures 11(b) and (c), 22.8% of γ_l in the localised right step cluster are above 0.8, but only 6.8% are above 0.8 in the localised left step cluster. Similarly, 27.5% of γ_r in the localised left step cluster are above 0.8, while 5.3% are above 0.8 in the localised right step cluster. The width $\gamma = 0.5$ corresponds to the minimal ground-state energy of a field free single-centre soft-core potential with our current parameters, and the vast majority of step functions have a γ value that is within the range [0.2:0.8]. As γ deviates from 0.5, part of the initial wavepacket bleeds out of the bound region despite being initially localised. This leads to oscillations during the flat 'step' portion of the autocorrelation function and explains the absence of initial wavepacket widths γ above 0.8 in the step clusters.

The other set of parameters symmetric with respect to the left/right direction are the molecular weights Z_l and Z_r.
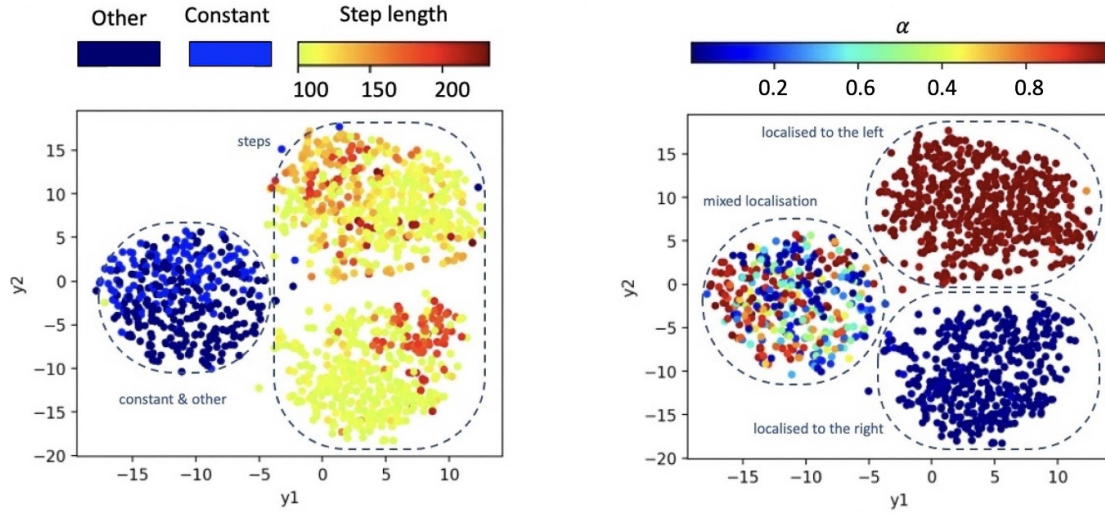
Figure 9. Plot of the 1332 12-dimensional data points that have been projected onto two axis y_1 and y_2 using the t-SNE dimensionality reduction technique described in section 2.2. Each subplot has the projected data plotted as a function of an initial input parameter (shown by the colour bar). All units are in (a.u.). unless stated otherwise. The input parameters shown in this figure are (a) The step function shape obtained by the sorting algorithm in section 3.1 that outputs 'constant', 'other', or the length of the step in the autocorrelation function and (b) The initial electron wavepacket localisation represented by the parameter α in equation (7). The full list of input parameters as well as details on the initial data set used can be found in section 2.2. PCA distributions using 500 000 data points are shown in appendix.

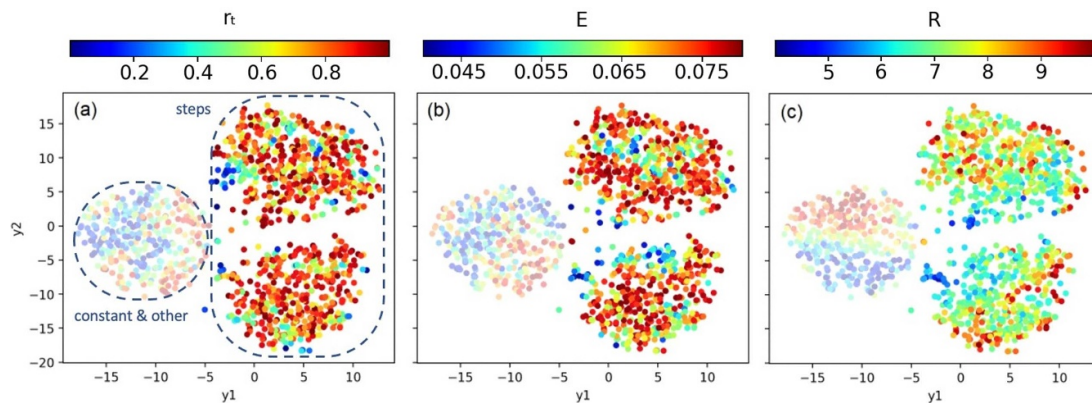**Figure 10.** Plot of the 1332 12-dimensional data points that have been projected onto two axis y_1 and y_2 using the t-SNE dimensional reduction technique described in section 2.2. Each subplot has the projected data plotted as a function an initial input parameter (shown by the colour bar). All units are in (a.u.). unless stated otherwise. The input parameter shown in this figure are (a) The ratio r_t between the two colour field amplitudes, (b) the overall field amplitude E_0 in equation (4) and (c) the internuclear distance R. The full list of input parameters as well as details on the initial data points used can be found in section 2.2. PCA distributions using 500 000 data points have been checked for accuracy (not shown).

Their effect on one cluster should be mirrored on the other. From figures 11(d) and (e), while there is no clear connection between the localised left cluster and Z_r, Z_l is more likely to be close to 1.0 (and vice-versa). Indeed there are 42% of data points that have $Z_l < 1.2$ in the localised right cluster, but 70% in the localised left cluster. Similarly, 39% of data points have $Z_r < 1.2$ in the localised left cluster, but 67% in the localised right cluster. This is further investigated in section 5.2.2.

5.1.4. Link between different parameters and the step length.
Going back to the distribution with respect to the autocorrelation function type in figure 9, those two 'step' clusters are then also distinguished into regions of 'short' (less than 150 a.u., or lime yellow) and 'long' (more than 150 a.u., or orange/red)

step length. From figure 12, we can already glean that the field-frequency ratio b affects the step length. However, there is no clear link with the field offset ϕ. This is further expanded upon in section 5.2.3.

5.2. Analysis of the step functions

In order to obtain a controlled burst of ionisation, two prerequisites are needed: First, a time interval in which the population stays bounded, and, second, a short burst of enhanced ionisation. Following the conclusions drawn from section 5.1, we already know what parameter range is required or preferred. In this section, we will provide an intuitive, physics-based analysis for the controlled-ionisation burst conditions.
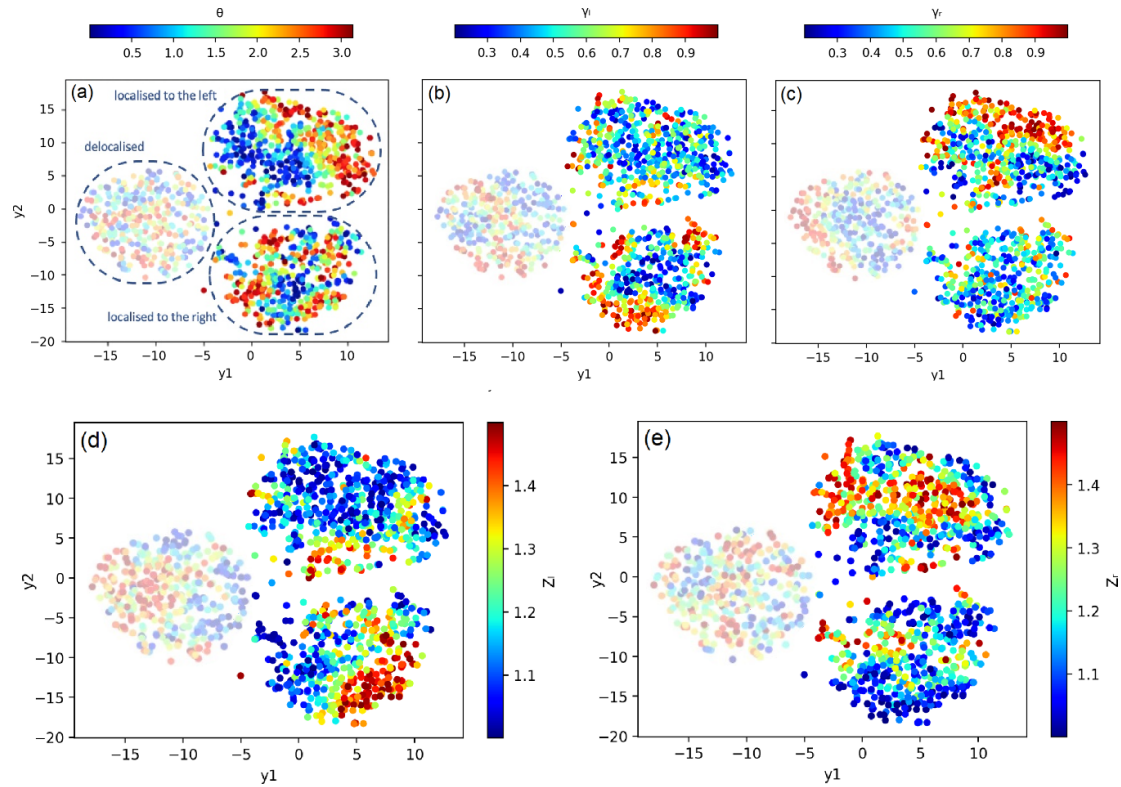
Figure 11. Plot of the 1332 12-dimensional data points that have been projected onto two axis y_1 and y_2 using the t-SNE dimensionality reduction technique described in section 2.2. Each subplot has the projected data plotted as a function an initial input parameter (shown by the colour bar). All units are in (a.u.). unless stated otherwise. The input parameters shown in this figure are (a) the phase difference between the left and right initial wavepackets θ, (b) the left initial wavepacket width γ_l, (c) the right wavepacket width γ_r, (d) the left molecular well depth Z_l and (e) the right molecular well depth Z_r. The full list of input parameters as well as details on the initial data points used can be found in section 2.2. PCA distributions using 500 000 data points have been checked for accuracy (not shown).
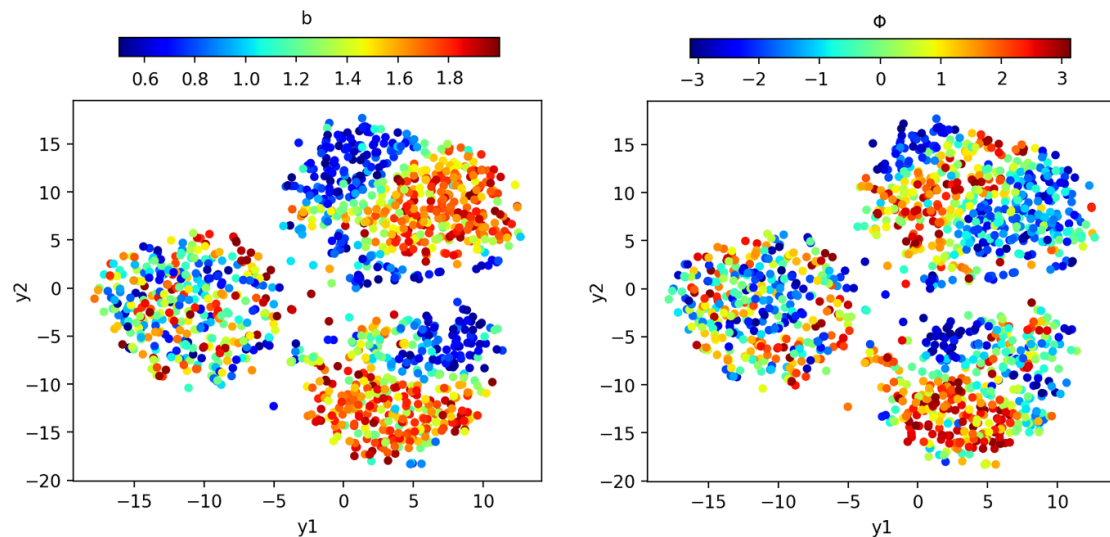

Figure 12. Plot of the 1332 12-dimensional data points that have been projected onto two axis y_1 and y_2 using the t-SNE dimensionality reduction technique described in section 2.2. Each subplot has the projected data plotted as a function of an initial input parameter (shown by the colour bar). All units are in (a.u.) unless stated otherwise. The input parameters shown in this figure are (a) The field-frequency ratio b and (b) the field offset ϕ in equation (4). The full list of input parameters as well as details on the initial data points used can be found in section 2.2. PCA distributions using 500 000 data points have been checked for accuracy (not shown).
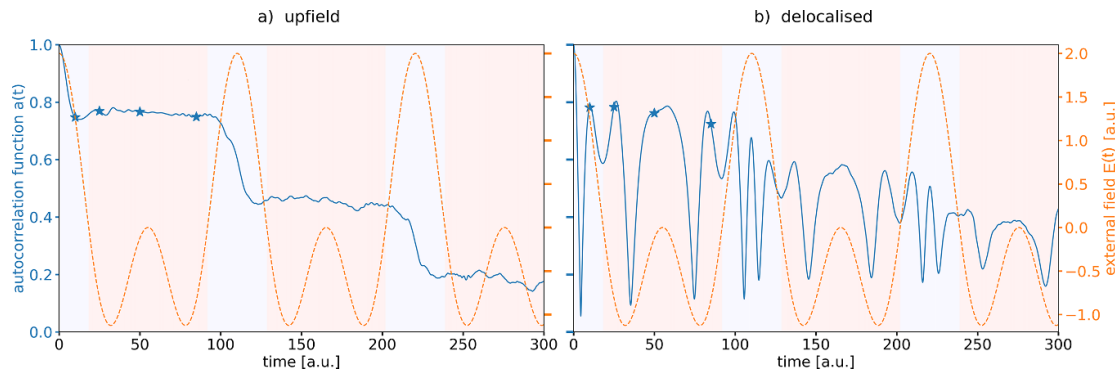
Figure 13. Comparison of auto-correlation functions at $R = 6.8$ a.u. with initial wavepacket localised upfield or delocalised. Direction of the field is denoted by the colour of the background, blue regions are positive values, pink are negative. The field is shown as the orange dashed lines with values shown on the rightmost y-axis and has form $E \propto \cos \omega t + \cos 2\omega t$ where $\omega = 0.057$ a.u. The stars denote autocorrelation function values at times $t = 10$ a.u., $t = 25$ a.u., $t = 50$ a.u., and $t = 85$ a.u..

5.2.1. Electron localisation.　　From figure 9, it is clear that the initial electron wavepacket must be localised, either around the left or right molecular well. Figure 13 illustrates the difference between using an initial localised wavepacket and a delocalised wavepacket. This, along with the Wigner function shown in figure 14, allows us to understand the mechanism behind the controlled ionisation release.

To obtain a burst of enhanced ionisation, the system must be in an optimal configuration. This was initially found in a study using static fields in [35], and further expanded upon in section 4. A key point is that the initial wavepacket must be localised upfield. This allows the population to escape directly through the quantum bridge to the semiclassical escape pathway and ultimately the continuum. It also stops the quantum bridge from cycling through the momentum space and bringing the population back to the upfield centre. Similarly, the population must stay bounded for an interval of time, meaning that the system must be in the configuration with lowest ionisation rate. As seen in figure 4, for static fields, this happens when the initial wavepacket is localised downfield. For the time dependent polychromatic field, the terms 'upfield' and 'downfield' become relative as the configuration changes with the direction of the field. However in either case the initial wavepacket must be localised on one of the molecular centres. As seen in the behaviour of the Wigner function in figure 14(right column) these two conditions are not possible if the initial wavepacket is delocalised. Because of the quantum interference in between the two molecular centres, there is always the cyclic motion of the quantum bridge.

The localisation of the wavepacket must work in conjunction with the sign of the external field for the stepwise behaviour to be present in the autocorrelation function. If the wavepacket is localised to the left and the external field $E(t)$ is positive, or if the wavepacket is localised to the right and $E(t)$ is negative, this will result in downfield localisation. Alternatively, upfield localisation occurs for a wavepacket localised to the left and negative $E(t)$, or a wavepacket localised to the right and positive $E(t)$.

In order to obtain a step function, the localisation must be upfield during the drop and downfield during the flat part of the step. In figure 13, the different field signs are shown by the different coloured shaded areas. Indeed, during the initial drop, the external field is positive and the population localised to the right, and therefore upfield. It escapes rapidly through the quantum bridge as seen by the Wigner function in figure 14(a) and the separatrices are open. As soon as the field changes sign, the approximately constant behaviour in the autocorrelation function begins. As seen in figures 14(b)–(d), during that time the wavepacket localisation is now downfield. Because of that, despite the separatrices being sometimes open, like in subplots (b) and (d), ionisation is suppressed. When the field is no longer strongly negative around $t = 60$, the separatrices are closed, as shown in subplot (c). This also stops the population from escaping. The autocorrelation function therefore has a step until the field becomes positive again, with the separatrices strongly open. From this analysis and the clustering obtained by the t-SNE distribution, it is clear the electron localisation is the most important parameter in obtaining a controlled ionisation release.

5.2.2. Separatrices.　　On top of the electron localisation, the presence of step functions is strongly dependent on the value of E_0, r_t, Z_l, Z_r and R, as seen in figures 10 and 11. Both E_0 and r_t have a similar effect on the external laser field: when r_t is close to 1.0 and when E_0 is large, the field peak increases in absolute value. As shown in figure 8, when using a static field, increasing E_0 leads to higher ionisation yield. In our time-dependent case, when E_0 or r_t is high, the value of ΔE at the field peak is much higher, meaning the separatrices are wide open. This phenomenon is best seen in figure 15 for a fixed value of R. In the second row it is clear that the increase in E_0 leads to higher maximum values of ΔE. For example, at internuclear distance $R = 10$, $E_0 = 0.04$ has $\Delta E = 0.7$ at the field maximum, while $E_0 = 0.08$ has $\Delta E = 1.6$. Compared to the corresponding autocorrelation functions in the first row, we see that when matched by the correct electron localisation, this will lead too a much steeper drop during the decreasing part of the autocorrelation function step. Using our previous example, at $E_0 = 0.04$ the first step plateaus at 0.9, while $E_0 = 0.08$ at 0.5.
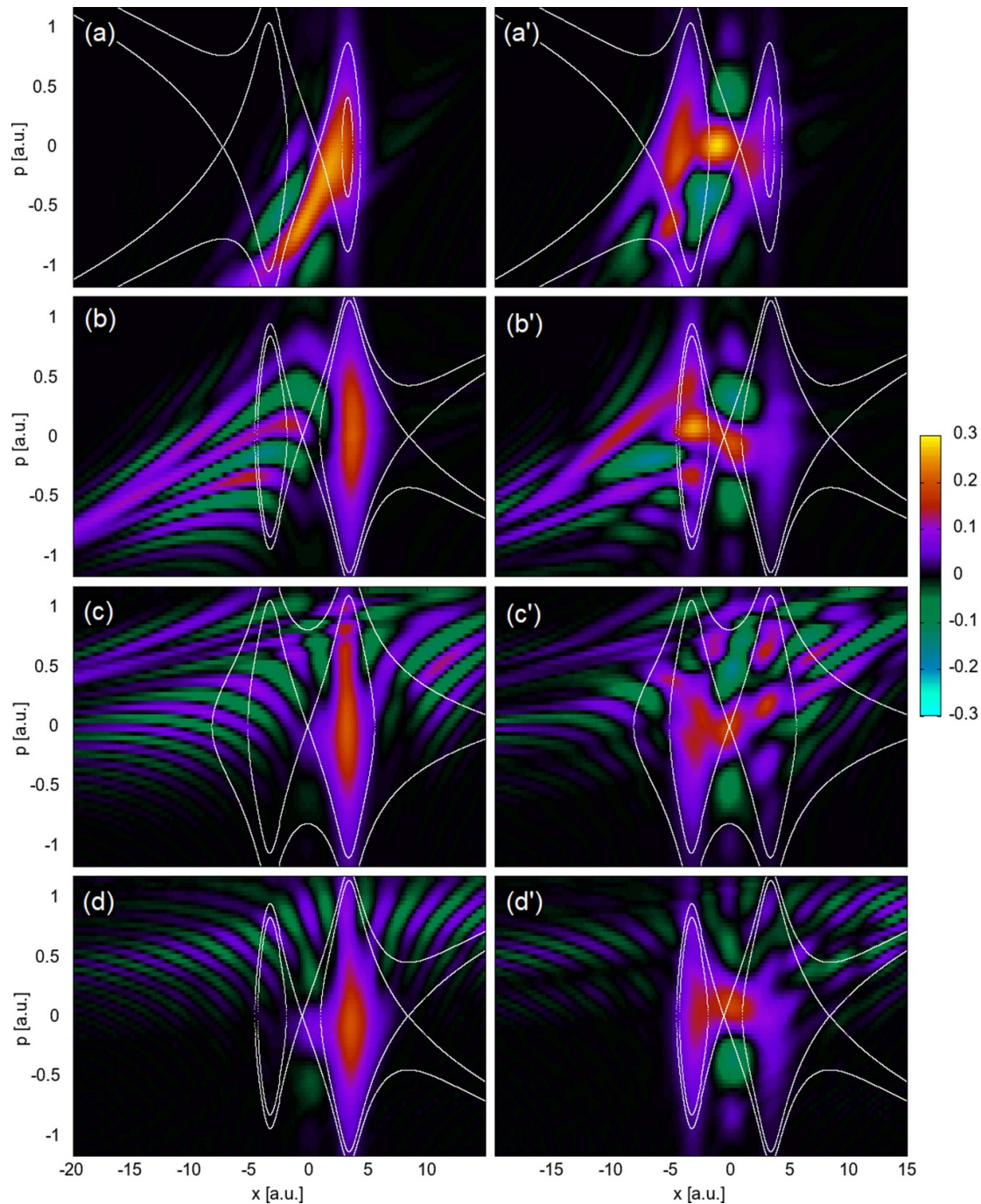
Figure 14. Wigner quasiprobability distributions computed for internuclear distances $R = 6.8$ a.u. with initial wavepacket localised at the right potential well ($\alpha = 0.0$) (left column) or delocalised between the two molecular wells ($\alpha = 0.5$) (right column). The external field has frequency $\omega = 0.057$ a.u. and strength $E_0 = 0.0534$ a.u.. The snap shots are taken at times $t = 10$ a.u. for (a) and (a'), $t = 25$ a.u. for (b) and (b'), $t = 50$ a.u. for (c) and (c'), and $t = 85$ a.u. for (d) and (d'). These times are indicated by stars in figure 13.

The effect of the internuclear distance R is at a glance not clear. When focusing on the initial drop, the connection between ΔE and the initial drop of the correlation seem contradictory. Intuitively one would expect a that a higher maximum ΔE lead to a steeper drop of the autocorrelation function, as was the case for varying r_t and E_0. But the opposite appears true with varying R. This is understood by results in [35], and illustrated in figure 15. As R is becomes too large, the quantum bridge between the two molecular wells weakens

and the ionisation rate falls. As consequence the initial drop of the autocorrelation function is low. With E_0 being low as well, this leads to a 'constant' autocorrelation function as seen in figure 15 for $R = 10$ and $E = 0.04$. When R is too small, the quantum bridges between the molecular wells are at their strongest, and initially facilitate population transfer, leading to a steeper drop. However, as seen in section 4, a small R does not lead to a high ionisation rate. That is understood in results from [35], and illustrated by the Wigner functions in figure 16:
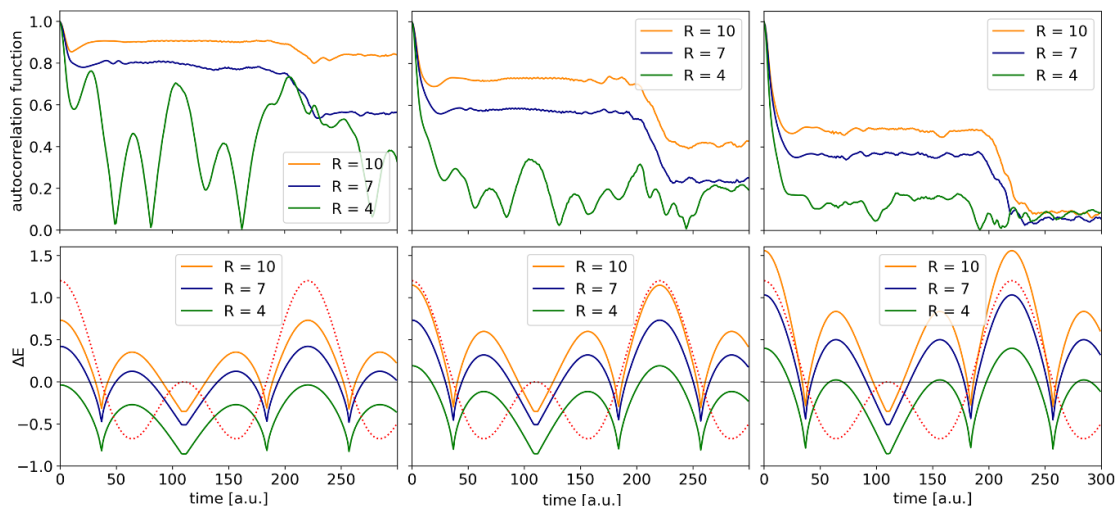
Figure 15. Different plots of autocorrelation functions (Top row) and ΔE (Bottom row) for $R = 4$ a.u., $R = 7$ a.u. and $R = 10$ a.u. with (left column) $E_0 = 0.04$ a.u., (Middle column) $E_0 = 0.06$ a.u. and (right column) $E_0 = 0.08$ a.u.. The external laser field is represented by the red dotted line (not to scale). We consider an initial wavepacket localised to the right, with $\gamma_r = 0.5$, and equal molecular weights $Z_r = Z_l = 1.0$. The external field amplitude and frequency ratios are $r_t = 1.0$ and $b = 0.5$, respectively.
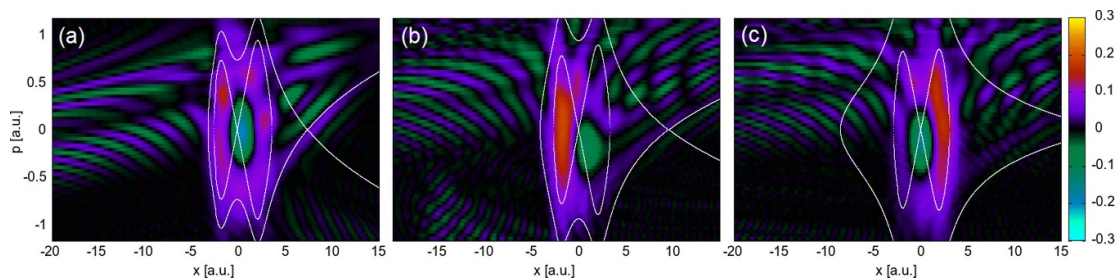

Figure 16. Evolution of the Wigner function with internuclear distance $R = 4$ a.u. and external field parameters $r_t = 1.0$, $b = 0.5$ and $E_0 = 0.04$ a.u.. The snap shots are taken at times (a) $t = 65$ a.u., (b) $t = 85$ a.u. and (c) $t = 100$ a.u.. Initial wavepacket localised to the right, with $\gamma_r = 0.5$. Molecular weights $Z_r = Z_l = 1.0$.

the quantum bridge brings population back to the right-side core. This cyclic motion does not follow the direction of the external field. As a consequence, the quasiprobability distribution does not stay within one centre during the 'flat' portion of the step autocorrelation function, as illustrated in figure 15.

While the effect of Z_l and Z_r differs greatly depending on the step cluster analysed, it is mirrored, so conclusions on one can be expanded to both. Focusing on the initially localised to the right cluster from figure 11, we see that while Z_l has little influence, the vast majority of step autocorrelation functions has $Z_r < 1.2$. This is illustrated in figure 17: The initial drop of the step autocorrelation function greatly reduces as Z_r increases. From the corresponding ΔE plot, the peak separatrix energy difference goes from 0.7 for $Z_r = 1.0$ to 0.6 for $Z_r = 1.5$. Compared to the effect of the separatrix energy difference of E_0 and its effect on the initial autocorrelation function drop, it appears something else must be at play. A better understanding is obtained when looking at the ionisation rate in static fields as a function of Z_r and Z_l. As explained in section 4.1, the biggest difference between figure 6 is not the separatrix energy difference, but the range of the bound region, especially in the momentum space. Back to the time dependent situation, as Z_r increases the population (here initially localised to the right)

stays trapped at the right molecular well, and the initial step drop will be much shorter.

5.2.3. Step length and two colour field frequencies. From figure 12 we can already observe that the step length is connected to the value of the two colour field frequency ratio b. Indeed, while step functions of step length less than 110 (a.u.) have on average $b = 1.5$, step function of step length greater than 150 (a.u.) have on average $b = 0.9$.

In order to view the relationship between the step length and other parameters in greater detail, we will now fix certain parameters in order to get a clearer picture of the effect the others, as well as only conserve data points with 'step' autocorrelation functions. First, we will start with the initial wavepacket localised at the right centre. This is equivalent to focusing only on the 'localised to the right' cluster of figure 9. Because of this, we also remove the initial wavepacket width γ_l and θ parameters. Finally, we will fix the field strength to $E_0 = 0.07$ a.u.. These results are shown in figure 18.

The t-SNE algorithm separates the data into four different clusters. The C1 and C3 clusters represent step lengths between 110 and 260. They are distinguished by the value of
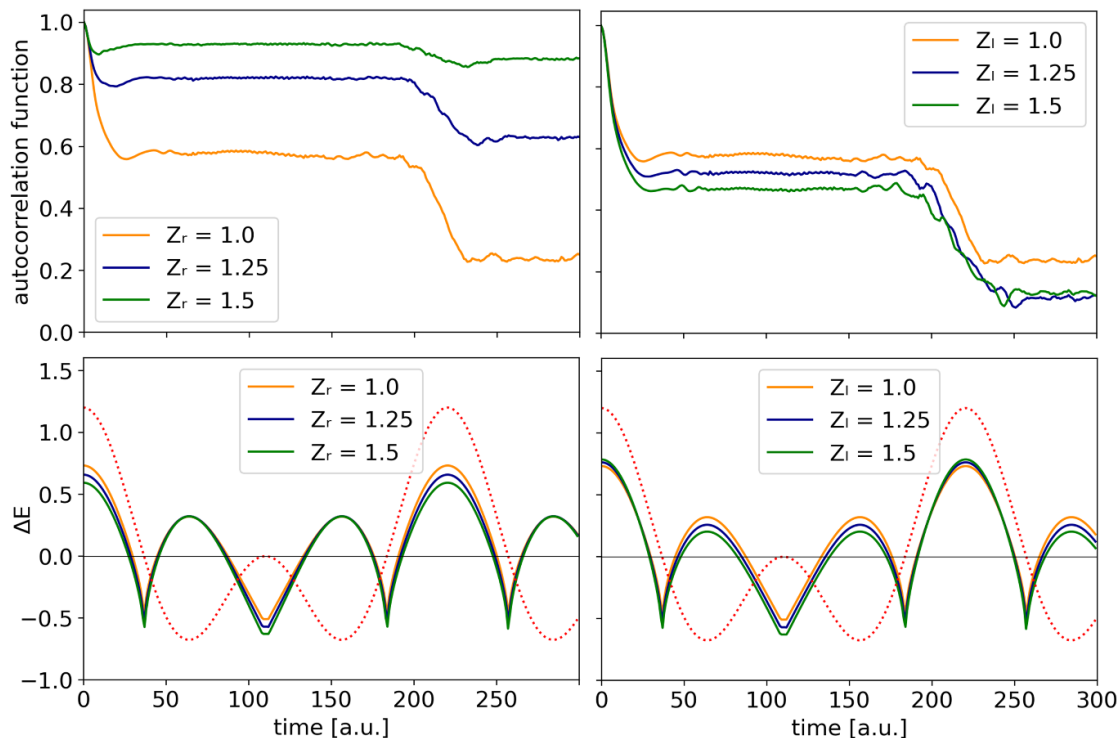
Figure 17. Different plots of autocorrelation functions and ΔE for (left column) $Z_r = 1.0$ a.u., $Z_r = 1.25$ a.u. and $Z_r = 1.5$ a.u. with $Z_l = 1.0$ a.u.. and (right column) $Z_l = 1.0$ a.u., $Z_l = 1.25$ a.u. and $Z_l = 1.5$ a.u. with $Z_r = 1.0$ a.u.. The initial wavepacket is localised to the right and other parameters are set to $R = 7$ a.u., $E = 0.06$ a.u., $r_t = 1.0$ and $b = 0.5$. The external laser field is represented by the red dotted line (not to scale).
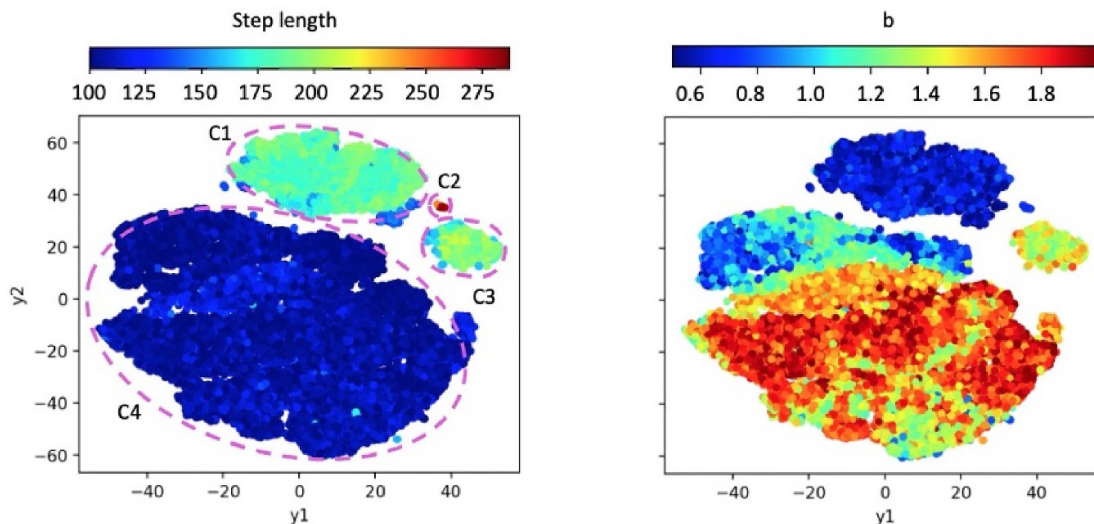

Figure 18. Plot of the 27 194 8-dimensional data points that have been projected onto two axis y_1 and y_2 using the t-SNE dimensional reduction technique described in section 2.2. All units are in (a.u.). unless stated otherwise. Each subplot has the projected data plotted as a function a initial input parameter. The initial input parameters include (a) The output of the step function algorithm from section 3.1 that is the length of the step in the autocorrelation function and (b) the frequency-ratio of the second colour field b as well as not shown here the offset of the second field ϕ, the field ratio r_t, the internuclear distance R, the left molecular well depth Z_l, the right molecular well depth Z_r, the right initial wavepacket width γ_r. All data points use an initially localised to the right wavepacket with $E_0 = 0.07$ a.u.. The input data set has been reduced from 1 000 000 data points to only look at step autocorrelation functions. PCA distributions using the original 1 000 000 data points have been analysed for accuracy (not shown).
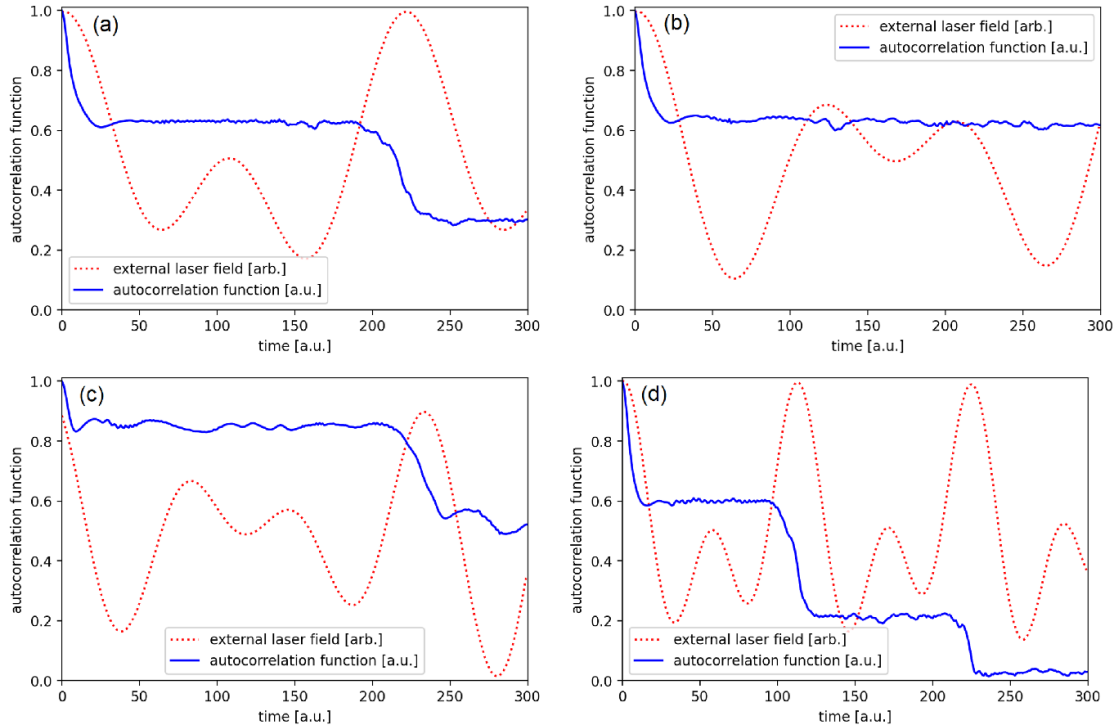
Figure 19. Plot of the corresponding autocorrelation function and external field in each of the four different clusters in figure 18, in order of increasing field frequency ration b. Constant parameters are $E_0 = 0.07 a.u.$, $R = 7$ a.u., $\alpha = 0.0$, $\gamma_r = 0.5$. The parameters used in each subplot are (a) from C1; $b = 0.5$, $r_t = 1.0$, $\phi = -0.2$, $Z_r = 1.2$ and $Z_l = 1.2$, (b) from C2; $b = 0.7$, $r_t = 1.0$, $\phi = -0.2$, $Z_r = 1.2$ and $Z_l = 1.2$, (c) from C3; $b = 1.3$, $r_t = 1.0$, $\phi = 1.0$, $Z_r = 1.1$ and $Z_l = 1.1$ and (d) from C4; $b = 2.0$, $r_t = 1.0$, $\phi = -0.13$, $Z_r = 1.05$ and $Z_l = 1.5$.

the frequency ratio b of the two-color fields: the largest C1 having an average of $b = 0.65$ and the smallest C3 $b = 1.32$. Next, the C2 cluster is the smallest and corresponds to all autocorrelation functions with a very long (greater than 260) step length. Finally, the C4 cluster is the largest cluster and corresponds to all autocorrelation functions with a short step length. Here the average step length is 1.09. An example of autocorrelation function and external field within each cluster is shown in figure 19.

As seen in the previous sections, the temporal location of the field peak, when matched with the population localisation, determines the step drop. From this, we can assume that the specific times for which the field peaks occur match the step length. This can be seen in figures 19(a) and (b), when increasing the second field frequency-ratio from $b = 0.5$ to $b = 0.7$, the distance between two field peaks increases and the step length goes from 187 to 285. This is also confirmed when looking at an example step function from clusters (c) and (d): The distance between field peaks matches the step length.

6. Conclusions

In this work we use dimensionality reduction techniques, namely the t-SNE method and PCA to investigate the effect of multiple parameters at once in enhanced ionisation. We show how quantum effects in strong-field ionisation of stretched diatomic molecules may be understood, classified and synchronised with the external laser field in order to create

tailored ionisation bursts. Thereby, the t-SNE was crucial to establish a hierarchy of parameters, and manipulate the relevant time scales. These time scales are either dictated by the field, or by the molecular system. The latter are associated to quantum-interference structures that provide a direct, intra-molecular population transfer via a quantum pathway in phase space, the quantum bridges [35, 58]. The results presented here have been mainly obtained with the t-SNE, while the PCA was used to rule out possible algorithm-dependent artefacts.

The effectiveness and accuracy of the t-SNE is first show-cased on the ionisation rate using a static field. The expected results are found using phase-space arguments and Wigner quasiprobability distributions. They completely match the conclusions drawn from the t-SNE distributions. Furthermore, a hierarchy in the importance of different parameters is quickly and effectively demonstrated. Because of this, we confidently used the t-SNE to project data of autocorrelation functions and their parameters for time-dependent fields. Using a two-colour field, we obtained a controlled ionisation release, which translates to a stepwise behaviour in the autocorrelation function. By using the t-SNE to project multi-dimensional data sets into 2 dimensions, ionisation profiles obtained while varying multiple parameters at once are organised and understood.

A conclusion from previous work [35] was that a key to understand enhanced ionisation is the interplay between the intra-molecular quantum bridges and the external field. This also holds for controlled ionisation release (represented by a step function in the autocorrelation function), where the

system requires a short burst of enhanced ionisation followed by a time interval for which the population stays bounded.

Quantum bridges are tied to many predictors for a step function in the autocorrelation function, including the strongest one: electron localisation. A delocalised initial wavepacket creates an interference pattern in both positive and negative momentum space. This leads to ionisation bursts that do not follow the external field. Therefore, we cannot obtain a time interval for which the population stays bounded. Moreover, the quantum bridges are highly tied to the internuclear distance. For that reason, configurations that suppress momentum gates do not lead to the burst of ionisation needed. This is the case when the internuclear distance is too large. Alternatively, a too small internuclear distance leads to cyclic motion in the momentum space, regardless of the initial state [35]. This also stops the population from staying bounded at one centre.

On the other hand, a higher field peak maximum leads to stronger ionisation bursts. A stronger field peak is achieved by increasing the field amplitude E_0 or adding a second field. This is neatly quantifiable by the separatrix energy difference ΔE. From this we determine bounded regions with closed separatrices and ionisation burst regions when the localisation is upfield with open separatrices. The timing of these field peaks matching with the upfield population lead to the start of the autocorrelation function drops. The field frequency determines the distance between the field peaks and is therefore the key to controlling the length of the steps. Finally, changing the molecular weights $Z_{r,1}$ affects the presence of step functions. As the upfield molecular weight increases, the upfield bound region increases and this greatly suppresses ionisation.

In summary, we can understand the physical cause and requirements for controlled ionisation release by separating the phenomenon into two steps, a short burst of enhanced ionisation and a time interval where the population stays bounded. For static fields, the optimal configuration for enhanced ionisation is pinpointed to an initial wavepacket localised upfield at optimal internuclear distance with a high intensity external field and a low upfield molecular weight. The separatrices are open with a high separatrix energy difference. This also holds during the time-dependent ionisation burst time interval, and will be periodic as the upfield and downfield configurations will change along with the sign of the external field, matching the field frequency. For the population to stay bounded, either the field strength must be low, separatrices closed or barely open, or the population must be localised in the downfield centre and therefore not follow the changes in the field strength and direction. In addition, the population must not cycle around through momentum gates, meaning the internuclear distance cannot be too short. The t-SNE was greatly effective at separating results into clusters and therefore visualising results due to specific combinations of parameters. For example, an overall analysis of the effect of Z_r on the step function autocorrelation function reveals only negligible effects. However, the step function results were separated into two clusters $\alpha < 0.2$ and $\alpha > 0.8$. The effect of the increased bound region and ionisation suppression from Z_r only affecting the $\alpha < 0.2$ cluster is brought into focus. Moreover, the t-SNE presented a hierarchy of the correlation

between different parameters and the quantity of study. From that, the role of electron localisation was pinpointed as the key parameter.

The importance of electron localisation is in agreement with the findings by several groups, reported over many years. In fact, resolving and ultimately controlling electron localisation in extended or dissociating molecules holds the promise of steering chemical reactions. This has led to many studies, both theoretical and experimental, employing, for instance, pump-probe schemes [7–9, 83–85], CEP stabilised few-cycle pulses [6, 86], long-wavelength fields [87, 88] or synthesised wave forms [89]. Moreover, orthogonally polarised fields have also been applied to trace or control the ionisation site [90–92]. Regarding enhanced ionisation, electron localisation in the upfield well, together with coupled charge-resonant states, were widely mentioned in the literature as major contributing factors. This holds both for seminal enhanced ionisation papers [36, 37] and more recent work in which models for time-dependent ionisation bursts have been developed [40, 57, 93, 94].

The techniques introduced in this work are general and thus may be applicable to other types of external fields and physical systems. Because the momentum gates are intrinsic to the system and caused primarily by quantum interference, instead of a non-adiabatic response to the field *per se*, effects such as sudden turn-ons are not necessary to give rise to the step-wise behavior discussed in the present work. Still, the external field can be tailored to alter the quantum bridges and trigger non-adiabatic responses that may aid or hinder the intra-molecular quasiprobability flow. Furthermore, the t-SNE can be applied to seek other patterns in the autocorrelation function or ionization rates, apart from the step-wise example studied here. Finally, since potential wells occur in a wide range of physical systems, the present techniques can be applied not only to more realistic molecular models, but also to solids and nanostructures. Thereby, a crucial issue would be to incorporate other degrees of freedom, multielectron dynamics and assess the role of decoherence. Loss of coherence can be caused by many physical mechanisms, such as coupling with additional degrees of freedom, intensity fluctuations, and incoherent emission from across the focal volume (for a brief discussion of some decoherence mechanisms in the context of strong-field quantum sensing see [95]). Recent studies using pump-probe schemes in H_2 have shown that coupling of electronic and vibrational degrees of freedom affects coherence and may hinder electron localisation [96]. Still, studies in large molecules indicate that phase relations may be preserved even in systems with many degrees of freedom [97], and could even be controlled leading to tailored ionisation enhancement or suppression [98]. Our simplified model is meant as a proof of concept and a first step towards more realistic scenarios.

Data availability statement

The data that support the findings of this study are available upon reasonable request from the authors.

Acknowledgments

Appendix. Principal component analysis

In this appendix we will present a few of the PCA results obtained throughout this study. The essence of PCA is to compute the principal components of a collection of points. The principal components are a sequence of unit vectors. The ith principal component is chosen such that its direction minimises the average squared distance from the data points to the principal component line, while being orthogonal to the previous $i-1$ vectors. Consequently, the first principal component can be defined as the direction that maximises the variance of the projected data. We can then use the first two principal components to perform a change of basis on the data. In other words, the aim of PCA is to compute the eigenvectors of the covariance matrix of the multidimensional data set and recast the data along the two largest eigenvectors.

Throughout this paper all t-SNE distributions were computed along with PCA distributions for comparison. In this appendix we present two examples, one from the static field analysis in section 4 and one from the time-dependent step autocorrelation function analysis in section 5, figures A1 and A2 respectively.

The PCA distribution in figure A1, obtained for the ionisation rate data set calculated using the static field, does not exhibit individual clusters corresponding to different ionisation rates. However, the distribution is organised following the different ionisation rates. From this we can see that both upfield electron localisation ($\alpha = 0$) and a right molecular weight $Z_r = 1.0$ lead to the highest ionisation rates.

When it comes to the time-dependent autocorrelation function, the PCA distribution in figure A2 does break into three distinct clusters corresponding to the different autocorrelation outputs: constant, step, and other. This allows us to draw similar conclusions to those obtained with the t-SNE, for instance that the electron must be localised to the right or left in order for the autocorrelation function to have a stepwise shape. However, contrary to the t-SNE distribution shown in figure 9, the step autocorrelation initially localised to the right data points and those initially localised to the left are not separated. That means that parameters that affect those two groups differently will not have their effect visually represented, for example Z_r and Z_l.
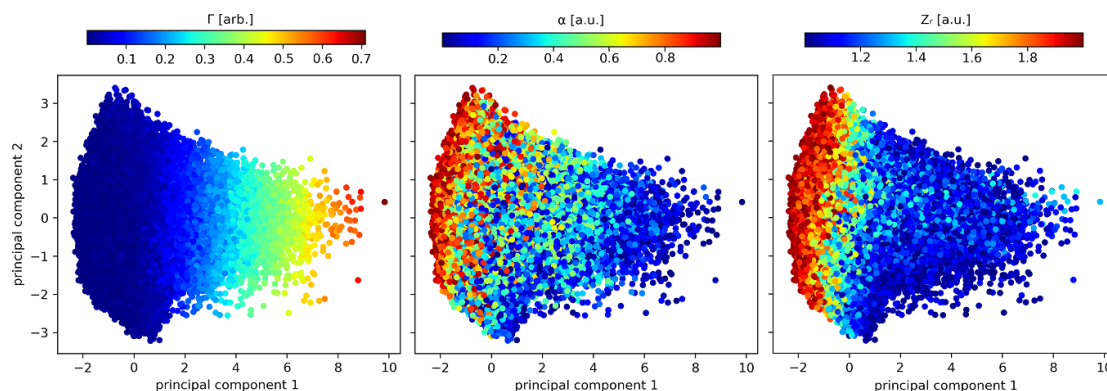
Figure A1. Plot of the 100 000 9-dimensional data points that have been projected onto their two principal component axis using PCA. The initial parameters used are equal to that of figure 8. Each subplot has the projected data plotted as a function an initial input parameter. The initial input parameters include (a) the ionisation rate Γ, (b) the electron localisation α and (c) the right molecular well depth Z_r.
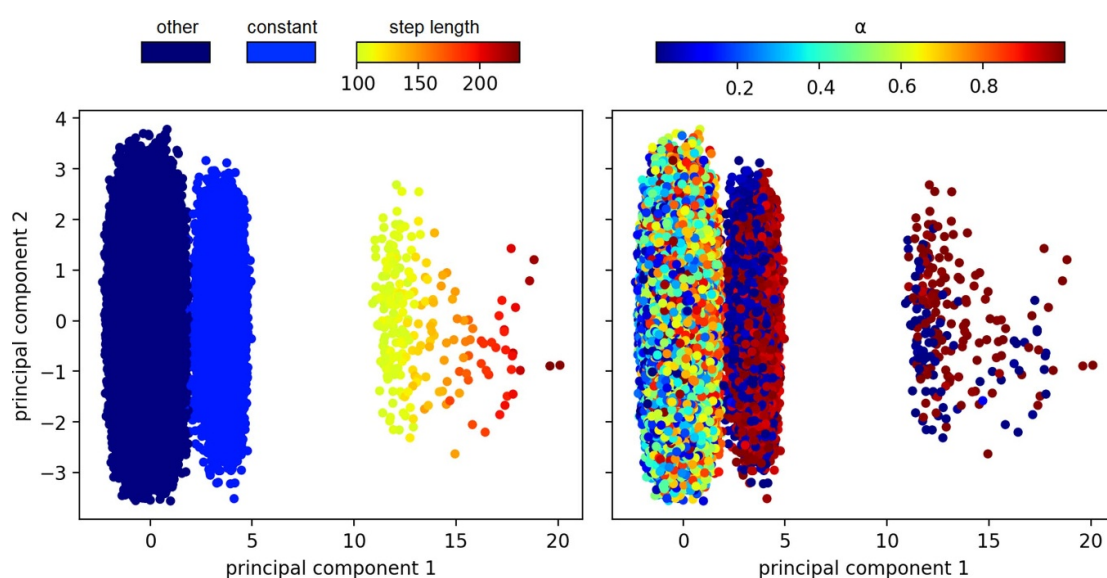

Figure A2. Plot of the 500 000 12-dimensional data points that have been projected onto their two principal component axis using PCA. The initial parameters used are equal to that of figure 9. Each subplot has the projected data plotted as a function an initial input parameter. The initial input parameters include (a) The step function shape obtained by the sorting algorithm in section 3.1 that outputs 'constant', 'other', or the length of the step in the autocorrelation function and (b) the electron localisation α.

ORCID iDs

J Dunham https://orcid.org/0000-0002-8068-0274
L Gover https://orcid.org/0000-0002-9278-5567
C Figueira de Morisson Faria https://orcid.org/0000-0001-8397-4529

References

[1] Shapiro M and Brumer P 2000 Coherent control of atomic, molecular and electronic processes *Advances In Atomic, Molecular and Optical Physics* vol 42), ed B Bederson and H Walther (New York: Academic) pp 287–345

[2] Bäuerle C, Glattli D C, Meunier T, Portier F, Roche P, Roulleau P, Takada S and Waintal X 2018 Coherent control of single electrons: a review of current progress *Rep. Prog. Phys.* **81** 056503

[3] Hikosaka Y, Kaneyasu T, Fujimoto M, Iwayama H and Katoh M 2019 Coherent control in the extreme ultraviolet and attosecond regime by synchrotron radiation *Nat. Commun.* **10** 4988

[4] Reiserer A and Rempe G 2015 Cavity-based quantum networks with single atoms and optical photons *Rev. Mod. Phys.* **87** 1379–418

[5] Peller D, Kastner L Z, Buchner T, Roelcke C, Albrecht F, Moll N, Huber R and Repp J 2020 Sub-cycle atomic-scale forces coherently control a single-molecule switch *Nature* **585** 58–62

[6] Kling M F *et al* 2006 Control of electron localization in molecular dissociation *Science* **312** 246–8

[7] Sansone G *et al* 2010 Electron localization following attosecond molecular photoionization *Nature* **465** 763–6

[8] Singh K P *et al* 2010 Control of electron localization in deuterium molecular ions using an attosecond pulse train and a many-cycle infrared pulse *Phys. Rev. Lett.* **104** 023001

[9] Xu H, Li Z, He F, Wang X, Atia-Tul-Noor A, Kielpinski D, Sang R T and Litvinyuk I V 2017 Observing electron localization in a dissociating H_2^+ molecule in real time *Nat. Commun.* **8** 15849

J. Phys. B: At. Mol. Opt. Phys. 55 (2022) 245501

H Chomet *et al*

[10] Cirac J I, Zoller P, Kimble H J and Mabuchi H 1997 Quantum state transfer and entanglement distribution among distant nodes in a quantum network *Phys. Rev. Lett.* **78** 3221–4

[11] Kimble H J 2008 The quantum internet *Nature* **453** 1023–30

[12] Wilde M M, McCracken J M and Mizel A 2010 Could light harvesting complexes exhibit non-classical effects at room temperature? *Proc. R. Soc.* A **466** 1347–63

[13] O'Reilly E J and Olaya-Castro A 2014 Non-classicality of the molecular vibrations assisting exciton energy transfer at room temperature *Nat. Commun.* **5** 3012

[14] Krausz F and Ivanov M 2009 Attosecond physics *Rev. Mod. Phys.* **81** 163–234

[15] Lépine F, Ivanov M Y and Vrakking M J J 2014 Attosecond molecular dynamics: fact or fiction? *Nat. Photon.* **8** 195

[16] Lein M 2007 Molecular imaging using recolliding electrons *J. Phys. B: At. Mol. Opt. Phys.* **40** R135

[17] Salières P, Maquet A, Haessler S, Caillat J and Taïeb R 2012 Imaging orbitals with attosecond and Ångström resolutions: toward attochemistry? *Rep. Prog. Phys.* **75** 062401

[18] Marangos J P 2016 Development of high harmonic generation spectroscopy of organic molecules and biomolecules *J. Phys. B: At. Mol. Opt. Phys.* **49** 132001

[19] Huismans Y *et al* 2011 Time-resolved holography *Science* **331** 61–65

[20] de Morisson Faria C F and Maxwell A S 2020 It is all about phases: ultrafast holographic photoelectron imaging *Rep. Prog. Phys.* **83** 034401

[21] Smirnova O, Mairesse Y, Patchkovskii S, Dudovich N, Villeneuve D, Corkum P and Ivanov M Y 2009 High harmonic interferometry of multi-electron dynamics in molecules *Nature* **460** 972–7

[22] Mairesse Y *et al* 2010 High harmonic spectroscopy of multichannel dynamics in strong-field ionization *Phys. Rev. Lett.* **104** 213601

[23] Calegari F *et al* 2014 Ultrafast electron dynamics in phenylalanine initiated by attosecond pulses *Science* **346** 336–9

[24] Kuleff A I, Kryzhevoi N V, Pernpointner M and Cederbaum L S 2016 Core ionization initiates subfemtosecond charge migration in the valence shell of molecules *Phys. Rev. Lett.* **117** 093002

[25] Calegari F, Trabattoni A, Palacios A, Ayuso D, Castrovilli M C, Greenwood J B, Decleva P, Martín F and Nisoli M 2016 Charge migration induced by attosecond pulses in bio-relevant molecules *J. Phys. B: At. Mol. Opt. Phys.* **49** 142001

[26] Ghimire S, Ndabashimiye G, DiChiara A D, Sistrunk E, Stockman M I, Agostini P, DiMauro L F and Reis D A 2014 Strong-field and attosecond physics in solids *J. Phys. B: At. Mol. Opt. Phys.* **47** 204030

[27] Vampa G *et al* 2018 Strong-field optoelectronics in solids *Nat. Photon.* **12** 465–8

[28] Yu C, Jiang S and Lu R 2019 High order harmonic generation in solids: a review on recent numerical methods *Adv. Phys.* X **4** 1562982

[29] Ortmann L and Landsman A S 2021 High-harmonic generation in solids *Advances In Atomic, Molecular and Optical Physics* vol 70, ed L F Dimauro, H Perrin and S F Yelin (New York: Academic) ch 2, pp 103–56

[30] Ciappina M F *et al* 2017 Attosecond physics at the nanoscale *Rep. Prog. Phys.* **80** 054401

[31] Ciappina M F and Lewenstein M 2019 *21st Century Nanoscience—A Handbook* (Boca Raton, FL: CRC Press)

[32] Schiffrin A *et al* 2013 Optical-field-induced current in dielectrics *Nature* **493** 70–74

[33] Schultze M *et al* 2013 Controlling dielectrics with the electric field of light *Nature* **493** 75–78

[34] Sommer A *et al* 2016 Attosecond nonlinear polarization and light–matter energy transfer in solids *Nature* **534** 86–90

[35] Chomet H, Sarkar D and de Morisson Faria C F 2019 Quantum bridges in phase space: interference and nonclassicality in strong-field enhanced ionisation *New. J. Phys.* **21** 123004

[36] Zuo T and Bandrauk A D 1995 Charge-resonance-enhanced ionization of diatomic molecular ions by intense lasers *Phys. Rev.* A **52** R2511–14

[37] Seideman T, Ivanov M Y and Corkum P B 1995 Role of electron localization in intense-field molecular ionization *Phys. Rev. Lett.* **75** 2819–22

[38] Wigner E 1932 On the quantum correction for thermodynamic equilibrium *Phys. Rev.* **40** 749–59

[39] He F, Becker A and Thumm U 2008 Strong-field modulated diffraction effects in the correlated electron-nuclear motion in dissociating H_2^+ *Phys. Rev. Lett.* **101** 213002

[40] Takemoto N and Becker A 2011 Time-resolved view on charge-resonance-enhanced ionization *Phys. Rev.* A **84** 023401

[41] Schleich W P 2011 *Quantum Optics in Phase Space* (New York: Wiley)

[42] Barnett S M and Radmore P M 2005 *Methods in Theoretical Quantum Optics* (Oxford: Clarendon)

[43] Leonhardt U 2010 *Essential Quantum Optics: From Quantum Measurements to Black Holes* (Cambridge: Cambridge University Press)

[44] Braunstein S L and van Loock P 2005 Quantum information with continuous variables *Rev. Mod. Phys.* **77** 513–77

[45] Serafini A 2017 *Quantum Continuous Variables: A Primer of Theoretical Methods* (Boca Raton, FL: CRC Press)

[46] Miller W H 2001 The semiclassical initial value representation: a potentially practical way for adding quantum effects to classical molecular dynamics simulations *J. Phys. Chem.* A **105** 2942–55

[47] Miller W H 2005 Quantum dynamics of complex molecular systems *Proc. Natl Acad. Sci.* **102** 6660–4

[48] Blakie P, Bradley A, Davis M, Ballagh R and Gardiner C 2008 Dynamics and statistical mechanics of ultra-cold Bose gases using c-field techniques *Adv. Phys.* **57** 363–455

[49] Chomet H and Figueira de Morisson Faria C 2021 Attoscience in phase space *Eur. Phys. J.* D **75** 201

[50] Czirják A, Kopold R, Becker W, Kleber M and Schleich W P 2000 The Wigner function for tunneling in a uniform static electric field *Opt. Commun.* **179** 29–38

[51] Zagoya C, Wu J, Ronto M, Shalashilin D and de Morisson Faria C F 2014 Quantum and semiclassical phase-space dynamics of a wave packet in strong fields using initial-value representations *New. J. Phys.* **16** 103040

[52] Gräfe S, Doose J and Burgdörfer J 2012 Quantum phase-space analysis of electronic rescattering dynamics in intense few-cycle laser fields *J. Phys. B: At. Mol. Opt. Phys.* **45** 055002

[53] Baumann C, Kull H-J and Fraiman G M 2015 Wigner representation of ionization and scattering in strong laser fields *Phys. Rev.* A **92** 063420

[54] Czirják A, Majorosi S, Kovács J and Benedict M G 2013 Emergence of oscillations in quantum entanglement during rescattering *Phys. Scr.* **T153** 014013

[55] Xu H, He F, Kielpinski D, Sang R T and Litvinyuk I V 2015 Experimental observation of the elusive double-peak structure in R-dependent strong-field ionization rate of H_2^+ *Sci. Rep.* **5** 13527

[56] Liu K and Barth I 2021 Distinguishing two mechanisms for enhanced ionization of H_2^+ using orthogonal two-color laser fields *Phys. Rev.* A **103** 013103

[57] Takemoto N and Becker A 2010 Multiple ionization bursts in laser-driven hydrogen molecular ion *Phys. Rev. Lett.* **105** 203004

[58] Kufel D, Chomet H and de Morisson Faria C F 2020 Alternative quantisation condition for wavepacket dynamics

in a hyperbolic double well *J. Phys. A: Math. Theor.* **54** 035304

[59] Balazs N and Voros A 1990 Wigner's function and tunneling *Ann. Phys., NY* **199** 123–40

[60] Hack S, Majorosi S, Benedict M G, Varró S and Czirják A 2021 Quantum interference in strong-field ionization by a linearly polarized laser pulse and its relevance to tunnel exit time and momentum *Phys. Rev.* A **104** L031102

[61] Dunjko V and Briegel H J 2018 Machine learning and artificial intelligence in the quantum domain: a review of recent progress *Rep. Prog. Phys.* **81** 074001

[62] Carleo G, Cirac I, Cranmer K, Daudet L, Schuld M, Tishby N, Vogt-Maranto L and Zdeborová L 2019 Machine learning and the physical sciences *Rev. Mod. Phys.* **91** 045002

[63] Carrasquilla J 2020 Machine learning for quantum matter *Adv. Phys.* X **5** 1797528

[64] Dawid A *et al* 2022 Modern applications of machine learning in quantum sciences (arXiv:2204.04198)

[65] Genty G, Salmela L, Dudley J M, Brunner D, Kokhanovskiy A, Kobtsev S and Turitsyn S K 2021 Machine learning and applications in ultrafast photonics *Nat. Photon.* **15** 91–101

[66] Chu C-T, Sheu Y-L and Chu S-I 2021 Bayesian optimal control of the ultrashort circularly polarized attosecond pulse generation by two-color polarization gating *Opt. Express* **29** 32900–9

[67] Liu X, Amini K, Sanchez A, Belsa B, Steinle T and Biegert J 2021 Machine learning for laser-induced electron diffraction imaging of molecular structures *Commun. Chem.* **4** 154

[68] Liu X, Zhang G, Li J, Shi G, Zhou M, Huang B, Tang Y, Song X and Yang W 2020 Deep learning for Feynman's path integral in strong-field time-dependent dynamics *Phys. Rev. Lett.* **124** 113202

[69] van der Maaten L and Hinton G 2008 Visualizing data using t-SNE *J. Mach. Learn. Res.* **9** 2579–605 (available at: http://jmlr.org/papers/v9/vandermaaten08a.html)

[70] Karl Pearson K 1901 LIII. On lines and planes of closest fit to systems of points in space *London, Edinburgh Dublin Phil. Mag. J. Sci.* **2** 559–72

[71] Feit M, Fleck Jr J and Steiger A 1982 Solution of the Schrödinger equation by a spectral method *J. Comput. Phys.* **47** 412–33

[72] Javanainen J, Eberly J H and Su Q 1988 Numerical simulations of multiphoton ionization and above-threshold electron spectra *Phys. Rev.* A **38** 3430

[73] Eberly J 1990 Scale variation in a one-dimensional model of an atom interacting with a strong laser field *Phys. Rev.* A **42** 5750

[74] Su Q and Eberly J 1991 Model atom for multiphoton physics *Phys. Rev.* A **44** 5997

[75] Rae S, Chen X and Burnett K 1994 Saturation of harmonic generation in one-and three-dimensional atoms *Phys. Rev.* A **50** 1946–9

[76] Majorosi S, Benedict M G and Czirják A 2018 Improved one-dimensional model potentials for strong-field simulations *Phys. Rev.* A **98** 023401

[77] Majorosi S, Benedict M G, Bogár F, Paragi G and Czirják A 2020 Density-based one-dimensional model potentials for strong-field simulations in He, H_2^+ and H_2 *Phys. Rev.* A **101** 023405

[78] Arrowsmith D and Place C 1992 *Dynamical Systems: Differential Equations, Maps and Chaotic Behaviour* (New York: Routledge)

[79] Weinbub J and Ferry D K 2018 Recent advances in Wigner function approaches *Appl. Phys. Rev.* **5** 041104

[80] Benedict M and Czirják A 1999 Wigner functions, squeezing properties and slow decoherence of a mesoscopic superposition of two-level atoms *Phys. Rev.* A **60** 4034

[81] Kullback S and Leibler R A 1951 On information and sufficiency *Ann. Math. Stat.* **22** 79–86

[82] Bottou L 1998 Online algorithms and stochastic approximations *Online Learning and Neural Networks* ed D Saad (Cambridge: Cambridge University Press)

[83] Yudin G L, Chelkowski S, Itatani J, Bandrauk A D and Corkum P B 2005 Attosecond photoionization of coherently coupled electronic states *Phys. Rev.* A **72** 051401

[84] He F, Ruiz C and Becker A 2007 Control of electron excitation and localization in the dissociation of H_2^+ and its isotopes using two sequential ultrashort laser pulses *Phys. Rev. Lett.* **99** 083002

[85] Wang Z, Liu K, Lan P and Lu P 2014 Control of electron localization in highly excited states with two ultraviolet laser pulses *J. Phys. B: At. Mol. Opt. Phys.* **48** 015601

[86] Roudnev V, Esry B D and Ben-Itzhak I 2004 Controlling HD^+ and H_2^+ dissociation with the carrier-envelope phase difference of an intense ultrashort laser pulse *Phys. Rev. Lett.* **93** 163601

[87] Liu K, Hong W, Zhang Q and Lu P 2011 Wavelength dependence of electron localization in the laser-driven dissociation of H_2^+ *Opt. Express* **19** 26359–69

[88] Liu K, Zhang Q, Lan P and Lu P 2013 Anomalous isotopic effect on electron-directed reactivity by a 3-μm midinfrared pulse *Opt. Express* **21** 5107–16

[89] Lan P, Takahashi E J and Midorikawa K 2012 Efficient control of electron localization by subcycle waveform synthesis *Phys. Rev.* A **86** 013418

[90] Wu J, Meckel M, Schmidt L, Kunitski M, Voss S, Sann H, Kim H, Jahnke T, Czasch A and Dörner R 2012 Probing the tunnelling site of electrons in strong field enhanced ionization of molecules *Nat. Commun.* **3** 1113

[91] Wu J, Meckel M, Voss S, Sann H, Kunitski M, Schmidt L P H, Czasch A, Kim H, Jahnke T and Dörner R 2012 Coulomb asymmetry in strong field multielectron ionization of diatomic molecules *Phys. Rev. Lett.* **108** 043002

[92] Liu K and Barth I 2017 Identifying the tunneling site in strong-field ionization of H_2^+ *Phys. Rev. Lett.* **119** 243204

[93] Kelkensberg F, Sansone G, Ivanov M Y and Vrakking M 2011 A semi-classical model of attosecond electron localization in dissociative ionization of hydrogen *Phys. Chem. Chem. Phys.* **13** 8647–52

[94] Takemoto N and Becker A 2011 Visualization and interpretation of attosecond electron dynamics in laser-driven hydrogen molecular ion using Bohmian trajectories *J. Chem. Phys.* **134** 074309

[95] Maxwell A S, Serafini A, Bose S and Figueira de Morisson Faria C 2021 Quantum estimation in strong fields: *in situ* ponderomotive sensing *Phys. Rev.* A **103** 043519

[96] Vrakking M J J 2021 Control of attosecond entanglement and coherence *Phys. Rev. Lett.* **126** 113203

[97] Delgado J, Lara-Astiaso M, González-Vázquez J, Decleva P, Palacios A and Martín F 2021 Molecular fragmentation as a way to reveal early electron dynamics induced by attosecond pulses *Faraday Discuss.* **228** 349–77

[98] Li S, Sierra-Costa D, Michie M J, Ben-Itzhak I and Dantus M 2020 Control of electron recollision and molecular nonsequential double ionization *Commun. Phys.* **3** 1–8